RSC Advances

PAPER

View Article Online
View Journal | View Issue

Cite this: *RSC Adv.*, 2026, **16**, 18861

First-principles optimization of thermoelectric and optoelectronic performance of $KSn_{1-x}Zn_xI_3$ ($x = 0$, 0.25, 0.5, 0.75, 1) perovskites for sustainable energy harvesting

Usama Ahmed,[a] Abu Sadat Md. Sayem Rahman, *[b] Jesia Alam Jui, [b] Md. Mukter Hossain, [a] Md. Mohi Uddin[a] and Md. Ashraf Ali [a]

In the pursuit of non-toxic and high-efficiency perovskite solar cell materials, this study investigates the enhancement of thermoelectric and optoelectronic properties of Zn-doped $KSn_{1-x}Zn_xI_3$ ($x = 0$, 0.25, 0.5, 0.75, 1) perovskites. The study uses first-principles density functional theory (DFT) with the Vienna *Ab initio* Simulation Package (VASP). Structural analysis confirms a transition from orthorhombic (*Pnma*) to monoclinic (*Pm*) phases. All the compositions exhibit thermodynamic, mechanical, and dynamic stability. Electronic properties reveal a robust bandgap range of 1.47–1.96 eV (GGA-PBEsol) and 2.34–3.02 eV (HSE06), positioning these materials as promising candidates for the top cell in a tandem solar cell and UV-optoelectronics. An indirect-to-direct band structure transition occurs at 50% Zn doping, which primarily enhances the stiffness, Pugh's ratio (2.39–2.70), and Poisson's (0.316–0.335) ratio of the lattice for $KSn_{1-x}Zn_xI_3$. The elastic modulus (E), shear modulus (G), and bulk modulus (B) in $KSn_{1-x}Zn_xI_3$ also significantly increased upon addition of Zn in the compound. These behaviors indicate that although there is better lattice stiffness in the material, there is still very good ductility for making flexible devices. Near-perfect mechanical isotropy has been achieved in $KZnI_3$ with a universal elastic anisotropy factor (A^U) of only 0.15. This low level of anisotropic elastic behavior indicates that $KZnI_3$ is unlikely to experience micro- fracture during or after manufacturing. Thermoelectric analysis shows that $KSnI_3$ maintained a high Seebeck coefficient of 230 μV K^{-1} at low temperature, while $KZnI_3$ showed a 225 μV K^{-1} Seebeck coefficient at elevated temperature. A high figure of merit (ZT) is achieved by both pristine compounds at high temperature, with values of 1.01 for $KSnI_3$ and 1.27 for $KZnI_3$. Furthermore, for optical properties, a high absorption coefficient of 7.32×10^5 cm^{-1} is observed by 25% Zn doping at UV-visible range. These findings make Zn-doped $KSnI_3$ perovskite material suitable for efficient, non-toxic, low-cost optoelectronic and thermoelectric devices.

Received 27th February 2026
Accepted 5th April 2026

DOI: 10.1039/d6ra01737a

rsc.li/rsc-advances

1. Introduction

Environmentalists have long been searching for new renewable energy sources. The growing demand for sustainable energy has driven researchers to develop new, eco-friendly novel materials. Scientists are looking for novel, eco-friendly materials that could convert sunlight to electricity by the photovoltaic effect.[1] In parallel, researchers are also looking for novel materials that can generate electricity from waste heat by the thermoelectric effect.[2] The ideal thermoelectric materials possess a large Seebeck coefficient, high electrical conductivity, and low thermal conductivity.[3] Such a type of combination can be achieved in semiconducting materials that are engineered with alloying elements. The perovskites are newly emerged semiconducting materials with the formula ABX_3, having good photovoltaic and thermoelectric properties.[1,4] Desired properties can be easily tailored by changing the composition of the perovskite material by alloying with appropriate elements. The perovskite solar cells (PSCs) introduced in 2009 had an initial power conversion efficiency (PCE) of 3.8%.[5] A significant advancement has been achieved in PCE value, which has increased to 26.7% over the past few years.[6] Although this remarkable gain in efficiency has been achieved within a short period, a question remains whether it is the most suitable perovskite combination for environmental and public health due to the toxic nature of lead (Pb).[7] To find solutions to this question, many researchers started to focus on much safer options than lead, such as Sn, Ge, Ti, Zn-based perovskite solar cells.[8–10] These Pb-free

[a]*Advanced Computational Materials Research Laboratory, Department of Physics, Chittagong University of Engineering & Technology (CUET), Chattogram 4349, Bangladesh*

[b]*Department of Materials and Metallurgical Engineering (MME), Chittagong University of Engineering & Technology (CUET), Chittagong 4349, Bangladesh. E-mail: mdsayem@cuet.ac.bd; Tel: +880 01318503244*

perovskite components have generated a lot of interest because of their improved optoelectronic behavior than Pb-based perovskite material. Compared to other non-toxic perovskite materials, Sn-based perovskites stand out due to their lower toxicity, ideal band gap, good charge transport properties, and potential for environmentally friendly energy solutions.[7,11] However, the easy oxidation process of Sn^{2+} to Sn^{4+} triggers p-type self-doping and generates Sn-vacancies. This phenomenon leads to Sn-based PSCs exhibiting inferior performance compared to Pb-based PSCs.[12] However, alloying with Ge at the B-site makes the Sn-based perovskite much more stable with improved efficiency.[13] At the same time, the development of non-toxic wide band gap perovskite is required for optoelectronic applications in the ultraviolet to the visible spectral range. The wide band gap perovskites have applications in the top cell of a tandem solar cell, UV-photodetectors, underwater photovoltaic devices, and light-emitting diodes (LEDs).[14–16]

To increase the stability and fine-tune the compositions of perovskites, various elements are introduced as dopants at the B-site of perovskite structures. Among the various elements employed for B-site doping in perovskite structures, transition-metal ions are particularly common. Typical examples include manganese (Mn^{2+}), zinc (Zn^{2+}), lead (Pb^{2+}), cadmium (Cd^{2+}), aluminum (Al^{3+}), tin (Sn^{2+}), nickel (Ni^{2+}), bismuth (Bi^{3+}), and Cerium (Ce^{3+}).[17] Among these different elements, comprehensive studies on zinc (Zn^{2+}) doping in perovskite compounds have established a pronounced effect on the photovoltaic and thermoelectric properties. The charge carrier collection efficiency and carrier lifetime in $MAPbI_3$ perovskite are improved by Zn doping. Additionally, it also promotes the formation of larger grains with fewer pinholes. This significantly reduces non-radiative recombination and suppresses hysteresis.[18,19] It is found in literature that the Sn-based perovskites are prone to intrinsic defects, undergo oxidation of Sn^{2+} to Sn^{4+}, and experience local lattice strain. However, Zn doping effectively mitigates these intrinsic defects and lattice distortions. At the same time, it enhances the carrier diffusion length in Sn-based perovskite films.[20] In general, higher oxidation resistance, low toxicity, and wide availability make zinc an excellent component for environmentally friendly solutions. Guo *et al.*[21] proposed a method to fabricate a hybrid perovskite material, which is eco-friendly and operationally reliable. Lead content can be reduced up to 50% by co-doping $CsPbBr_3$ with Zn and Mn without changing its optoelectronic properties. Kooijman *et al.*[22] also reported that incorporating zinc halide into Pb-based perovskites significantly enhances the structural integrity, film morphology, and crystallinity. In addition, the zinc modified perovskites solar cell exhibited improved luminescence and achieved about a 33% increase in solar cell efficiency compared with their undoped materials. In a similar study, Ou *et al.*,[23] where Zn^{2+} is added in $Cs_2AgBiBr_6$ instead of Ag, results in a high PCE value of 45.9% due to enhanced charge transport and more efficient interfacial charge extraction. Wei *et al.*[24] investigate that zinc doping in halide perovskites weakens nonadiabatic coupling in the conduction band, which in turn slows down hot-carrier cooling. This behavior suggests a viable path for improving the lives of hot carriers in forthcoming solar technology. All things considered, these investigations highlight zinc doping as a successful method for developing stable, high-performing, and eco-friendly perovskite-based optoelectronic devices.

The thermoelectric potential of K and Sn-based perovskite compounds has become the focus of recent studies by many research groups. For example, the double perovskite compounds $K_2CuBiBr_6$ and $K_2AgBiBr_6$ were studied by Ali *et al.*[25] These perovskite materials exhibit strong thermoelectric performance characterized by high Seebeck coefficients, good electrical conductivity, and *ZT* values of 0.84 for $K_2CuBiBr_6$ and 0.78 for $K_2AgBiBr_6$. Similarly, Abdullah and Gupta[26] reported that the double perovskites A_2GeSnF_6 (A = K, Rb, Cs) are outstanding thermoelectric candidates with *ZT* values in the range of 0.94–0.97. The literature report indicates that Sn-based oxide perovskite materials, such as $BaSnO_3$, exhibit excellent high temperature thermoelectric performance. In a study by Song *et al.*,[27] $BaSnO_3$ achieves a high p-type *ZT* of 1.52 and n-type *ZT* of 0.37 at 900 K due to its favorable electronic and thermal transport properties. The Zn-based perovskites, such as the inorganic cubic $CsZnX_3$ (X = F, Cl, Br, I) studied by Aqili *et al.*[28] also exhibit promising thermoelectric properties due to their favorable electronic and thermal transport characteristics. They observed that these compounds have $ZT > 0.7$ across a temperature range of 300–800 K, making them promising for thermoelectric applications. Similarly, Agouri *et al.*[29] computationally investigated the thermoelectric properties of cubic (space group $Pm\bar{3}m$, no. 221) $XZnI_3$ (X = Na, K, Rb, Cs) perovskites. They observed that these compounds are semiconductors with indirect band gaps in the range of 0.51–0.62 eV (TB-nmBJ) and *ZT* values reaching 0.55–0.66 at 1000 K. Specifically, the cubic $KZnI_3$ phase exhibited a *ZT* value of approximately 0.55 at 1000 K and a band gap of 0.606 eV, respectively. Numerous beneficial effects of Zn doping on thermoelectric properties are also reported in the literature. For instance, Zn-doping in GeTe introduces resonance states and increases the Seebeck coefficient value by raising the heavy hole valence band on top of the light hole valence band. Zn-doping also reduces the lattice thermal conductivity in GeTe and hence improves the overall *ZT* value.[30] The co-doping of Ge and Zn in SnTe is investigated by Shenoy *et al.*[31] The Ge doping in SnTe reduces the thermal conductivity. The Zn doping in SnTe suppresses the bipolar effect at elevated temperature by widening the band gap, distorts the density of states (DOS) near the Fermi level by creating resonance states, which ultimately improves the power factor by co-doping strategy. When Zn is co-doped with Bi in SnTe, it drastically reduces the lattice thermal conductivity and results in a peak *ZT* value of ~1.6 at elevated temperature.[32] When Zn is co-doped with Ag in SnTe, it gives a high *ZT* value of ~0.97 in the temperature range of 500 K to 840 K.[33] Therefore, the doping of Zn, significantly improves the thermoelectric performance. The effect of doping on the thermoelectric properties can be accurately identified with the help of density functional theory (DFT) analysis. The DFT is a reliable scientific tool to accurately predict experimental results. For instance, DFT predicted the increment in band gap

values due to Zn-doping from 0.079 eV to ~0.2 eV in the $Sn_{14}Zn_2Te_{16}$ compound. Experimentally, Zn-doped samples showed no "hump" in lattice thermal conductivity at high temperatures, unlike undoped SnTe. This confirms that the increased band gap due to Zn-doping prevented bipolar diffusion in SnTe.[34] In the case of Pb–Zn co-doping in SnTe, the DFT confirmed the increment in the experimental Seebeck coefficient values. DFT predicted Pb–Zn co-doping introduces resonance states near the Fermi level and raises the heavy hole valence band approximately 0.1 eV above the light hole valence band at room temperature. This DFT prediction is confirmed by the experimental result,[35] where because of the Pb–Zn co-doping in SnTe, significantly enhanced Seebeck coefficient value to 109 μV K^{-1} at 300 K and 229 μV K^{-1} at 840 K, respectively. In the case of Zn doping in $Pb_{0.6}Sn_{0.4}Te$,[36] undoped $Pb_{0.6}Sn_{0.4}Te$ has a zero band gap, which causes the Seebeck coefficient to drop after 570 K. DFT predicted that Zn opens a band gap (0.26 eV) in zero-gap $Pb_{0.6}Sn_{0.4}Te$. This is experimentally confirmed by the suppression of bipolar diffusion, evidenced by Seebeck values continuously increasing up to 840 K (221 μV K^{-1}). It is also observed from Boltzmann transport calculations that Zn-doping in SnTe improves the *ZT* value. Experimentally, $Sn_{0.96}Zn_{0.08}Te$ validated this by achieving a high *ZT* value of ~0.28 at 300 K and a peak *ZT* of ~1.49 at 840 K, respectively.[34] Therefore, the DFT prediction has a good match with the experimental observation of thermoelectric properties.

Among different perovskite compositions, the non-toxic $KSnI_3$ in its orthorhombic (*Pnma*) phase has been explored by different research groups for photovoltaic applications.[37–40] The advantage of using potassium (K^+) is that K^+ is more cost-effective than its cesium (Cs^+) and rubidium (Rb^+) counterparts.[8] The Zn is also non-toxic and earth abundant element. However, the use of Zn-doping at the B-site to stabilize the instability caused by Sn has remained largely unexplored for $KSnI_3$ perovskite. Inspired by the success of Zn-doping at the B-site of different perovskites, we hypothesize that Zn-doping at the B-site of $KSnI_3$ could synergistically enhance its multifunctional properties. Therefore, for the first time, this study employs density functional theory (DFT) to theoretically investigate the effect of Zn-doping on the structural, mechanical, electronic, optical, and thermoelectric properties of orthorhombic $KSnI_3$ perovskite. Our goals are to: (i) identify the effect of Zn-doping on thermoelectric transport coefficients and ultimately to evaluate *ZT*, and (ii) elucidate doping-induced changes in the band structure and optical absorption for UV-visible light applications. This work investigates the effect of Zn-doping on the properties of $KSnI_3$ perovskite for two distinct but equally important applications: (i) optoelectronics and (ii) thermoelectric. The optoelectronic properties are analyzed to determine the material's suitability to convert light to electricity. On the other hand, thermoelectric properties are studied independently to evaluate the potential of Zn-doped $KSnI_3$ perovskites in waste heat recovery. The focus of this analysis is to produce a nontoxic Zn-doped $KSnI_3$ perovskite material for advanced thermoelectric and optoelectronic applications.

2. Computational methodology

The density functional theory (DFT) calculations for the $KSn_xZn_{1-x}I_3$ perovskite compositions are carried out by using the Vienna *Ab initio* Simulation Package (VASP).[41] The Perdew–Burke–Ernzerhof for solids within the Generalized Gradient Approximation (GGA-PBEsol) functional is used to iteratively solve the Kohn–Sham equations in order to get the ground-state electronic structure.[42] The electronic band structure, density of states (DOS), optical properties, and thermoelectric properties of the material were all studied in detail using the hybrid Heyd–Scuseria–Ernzerhof (HSE06) functional.[43] The valence electron configurations included K ($3s^2$ $3p^6$ $4s^1$), Sn ($4d^{10}$ $5s^2$ $5p^2$), Zn ($3d^{10}$ $4s^2$), and I ($4d^{10}$ $5s^2$ $5p^5$). For structural optimization, the energy and ionic convergence conditions were established at 1×10^{-6} eV and -2×10^{-2} eV $Å^{-1}$, respectively. Monkhorst–Pack *k*-point meshes of $3 \times 7 \times 2$ are utilized to sample the Brillouin zone, with a plane-wave kinetic energy cutoff of 450 eV. The Self-Consistent Field (SCF) iteration is performed until convergence is achieved by updating the charge density and computing an effective potential to solve for a new wave function.[44] The calculation's post-processing analysis, including density of states (DOS), band structure, optical, and mechanical properties, is done using VASPKIT.[45] Thermoelectric transport parameters are calculated using Boltzmann's theory with the Boltztrap2 tool,[46] and the phonon dispersion is measured using the linear response method of the Cambridge Serial Total Energy Package (CASTEP) Code.[47] The crystal structures of the $KSn_xZn_{1-x}I_3$ perovskites are illustrated using the VESTA package.[48]

3. Results and discussion

3.1 Structural analysis

The perovskite structure (ABX_3) in which the $KSnI_3$ compound crystallizes, with K occupying the A-site, Sn at the B-site, and I at the X-site. The structure belongs to space group 62 and features an orthorhombic phase (*Pnma*).[49] The phase changes from an orthorhombic to a monoclinic phase when Zn replaces Sn with space group 6 (*Pm*). Table 1 shows the atomic configuration of $KSn_{1-x}Zn_xI_3$ perovskite compositions. Fig. 1 shows the schematic of the crystal structure of $KSn_{1-x}Zn_xI_3$ perovskites. The lattice parameter and unit cell volume are optimized using the GGA-PBESol approximation. Table 2 provides a summary of the optimal lattice parameters for the orthorhombic and monoclinic phases.

The Goldschmidt's tolerance factor (T_F) has been calculated to verify the stability of $KSn_{1-x}Zn_xI_3$ perovskite compounds. The following is the equation for T_F:[50,51]

$$T_F = \frac{R_A + R_X}{\sqrt{2}R_B + R_X}$$

The radii of K, B-site ions (Sn/Zn), and I are denoted as R_A, R_B, and R_X, respectively. These values are taken from the Shannon ionic radii.[52] As atomic size increases, the value of the tolerance factor (T_F) decreases. The probability of a stable

Table 1 Optimized Wyckoff positions and fractional atomic coordinates (*x*, *y*, *z*) of K, Sn/Zn, and I atoms in $KSn_{1-x}Zn_xI_3$ perovskites obtained from DFT structural relaxation

Compounds	K	Sn	Zn	I
$KSnI_3$ (orthorhombic)	(0.077304, 0.75, 0.672586)	(0.165021, 0.25, 0.941203)	—	(0.34052, 0.75, 0.011544), (0.017173, 0.25, 0.120918) and (0.30433, 0.25, 0.787371)
$KSn_{0.75}Zn_{0.25}I_3$ (monoclinic)	(0.077304, 0.75, 0.672586)	(0.836324, 0.5, 0.952061), (0.331516, 0.5, 0.556637) and (0.663123, 0, 0.439629)	(0.1746, 0.0000, 0.5537)	(0.34052, 0.75, 0.011544), (0.017173, 0.25, 0.120918) and (0.30433, 0.25, 0.787371)
$KSn_{0.5}Zn_{0.5}I_3$ (monoclinic)	(0.077304, 0.75, 0.672586)	(0.328786, 0.75, 0.549802) and (0.672324, 0.25, 0.452198)	(0.220023, 0.25, 0.02946) and (0.779967, 0.75, 0.97054)	(0.34052, 0.75, 0.011544), (0.017173, 0.25, 0.120918) and (0.30433, 0.25, 0.787371)
$KSn_{0.25}Zn_{0.75}I_3$ (monoclinic)	(0.077304, 0.75, 0.672586)	(0.661255, 0, 0.441198)	(0.164057, 0, 0.046774), (0.833688, 0.5, 0.94975) and (0.324833, 0.5, 0.568874)	(0.34052, 0.75, 0.011544), (0.017173, 0.25, 0.120918) and (0.30433, 0.25, 0.787371)
$KZnI_3$ (orthorhombic)	(0.077304, 0.75, 0.672586)	—	(0.165021, 0.25, 0.941203)	(0.34052, 0.75, 0.011544), (0.017173, 0.25, 0.120918) and (0.30433, 0.25, 0.787371)

perovskite structure is indicated by the T_F value, which ranges from 0.8 to 1.[53] Table 2 contains the calculated T_F values for $KSn_{1-x}Zn_xI_3$ perovskites.

By calculating its formation energy (ΔE_{form}), the chemical endurance of the semiconductor $KSn_{1-x}Zn_xI_3$ perovskites has been further evaluated. The formula, as presented in ref. 54, is summarized here.

$$\Delta E_{form} = \frac{E_{Total}^{KSn_{1-x}Zn_xI_3} - \left(AE_{solid}^{K} + BE_{solid}^{Sn} + CE_{solid}^{Zn} + DE_{solid}^{I}\right)}{A + B + C + D}$$

The number of K, Sn, Zn, and I atoms in the $KSn_{1-x}Zn_xI_3$ unit cell is represented by the variables *A*, *B*, *C*, and *D* in the provided equation. The total energy of the $KSn_{1-x}Zn_xI_3$ perovskite compound is denoted by the expressions $E_{Total}^{KSn_{1-x}Zn_xI_3}$ and the corresponding solid-state energies of K, Sn, Zn, and I atoms are denoted as; E_{solid}^{K}, E_{solid}^{Sn}, E_{solid}^{Zn}, and E_{solid}^{I}. The unit of the formation energy is eV per atom. The negative sign of the formation energy confirmed their stability. The computed formation energy values are shown in Table 2.

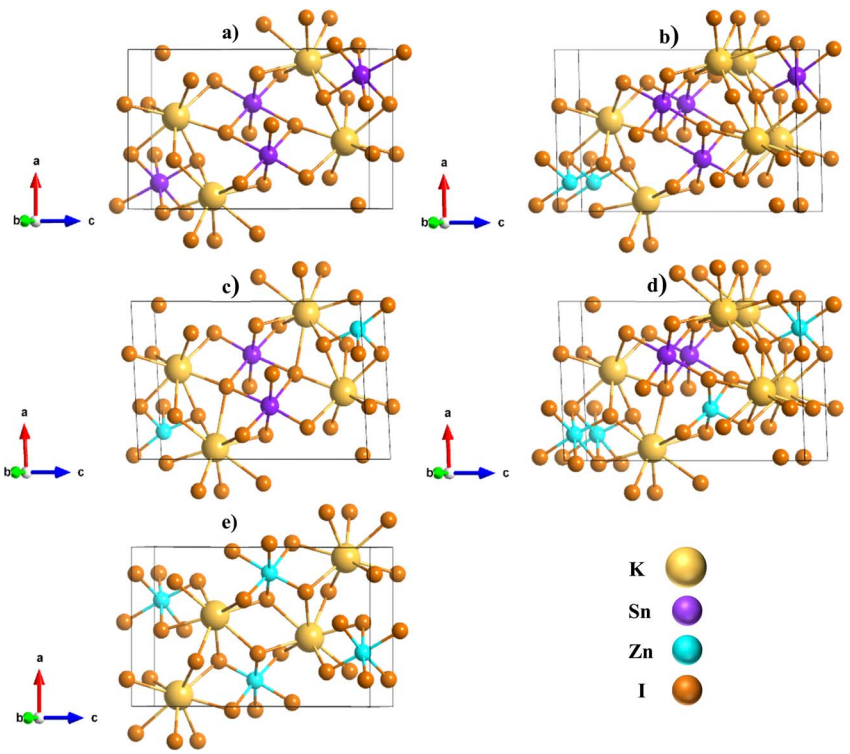

Fig. 1 The schematic representation of the unit cell structure of (a) $KSnI_3$, (b) $KSn_{0.75}Zn_{0.25}I_3$, (c) $KSn_{0.5}Zn_{0.5}I_3$, (d) $KSn_{0.25}Zn_{0.75}I_3$, and (e) $KZnI_3$ perovskite compounds.

Table 2 The optimized lattice parameters *a*, *b*, and *c* (Å), volume of unit cell *V* (Å^3), formation energy (ΔE_{form}), and tolerance factor (T_F) of $KSn_{1-x}Zn_xI_3$ perovskite compounds

Compounds	*a* (Å)	*b*(Å)	*c*(Å)	*V* (Å^3)	ΔE_{form} (eV per atom)	T_F	Ref.
$KSnI_3$	10.20	4.611	16.79	790.13	−1.333	0.93	This work
	10.45	4.71	17.00	—	—	—	49
$KSn_{0.75}Zn_{0.25}I_3$	10.16	4.52	16.55	759.33	−1.324	0.93	This work
$KSn_{0.5}Zn_{0.5}I_3$	10.04	4.50	16.25	734.95	−1.328	0.92	This work
$KSn_{0.25}Zn_{0.75}I_3$	10.04	4.30	16.26	703.74	−1.304	0.92	This work
$KZnI_3$	9.84	4.23	16.03	669.41	−1.304	0.92	This work

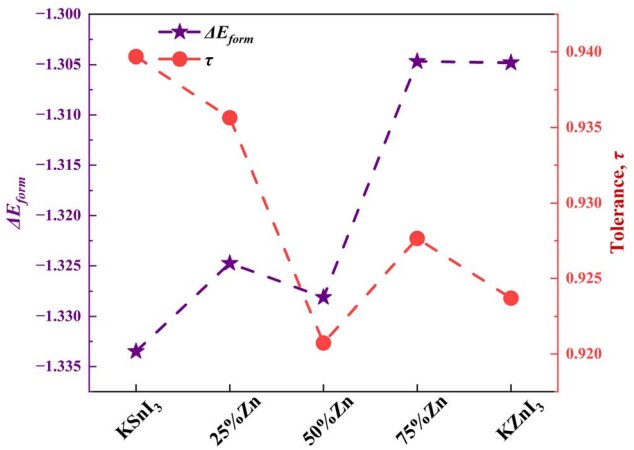

Fig. 2 Effect of Zn doping on formation energy (ΔE_{form}) and tolerance factor (τ) in $KSn_{1-x}Zn_xI_3$ perovskites.

Fig. 2 illustrates the change of Goldschmidt tolerance factor (τ) and formation energy (ΔE_{form}) with Zn content (x) in $KSn_{1-x}Zn_xI_3$ perovskites. For undoped $KSnI_3$ and 50% Zn doping ($x = 0.5$), formation energy causes the thermodynamic stability to peak, providing stability to the lattice at these doping concentrations. This is because the lattice is properly accommodated when smaller Zn^{2+} ions partially replace larger Sn^{2+} ions, reducing lattice strain and distortion. According to the ideal perovskite stability criterion, the tolerance factor shows a minimum at $x = 0.5$. Beyond this, the little departure from perfect ionic size matching causes τ to increase as Zn content keeps rising, resulting in a subtle asymmetry in the structure. These trends validate that intermediate Zn doping levels, in particular 50%, present maximum structural stability and maximum geometric compatibility in the lattice.

3.1.1 Dynamic stability. The phonon dispersion curves for $KSn_{1-x}Zn_xI_3$ are illustrated in Fig. 3(a–d) for the high-symmetry path *G*–*F*–*Q*–*Z*–*G*. The goal is to investigate dynamic stability and see how Zn substitution influences the lattice vibrations. The phonon dispersion for the parent compound, $KSnI_3$, has been assessed in ref. 49. For all Zn-doped compositions, the phonon spectra do not show any imaginary frequencies, indicating that each structure is dynamically stable. This indicates that the Zn substitution throughout the range should preserve the mechanical integrity of the perovskite lattice, suggesting that alloying is feasible without destabilizing the lattice. However, the slight imaginary frequencies observed near the *Z*-point in the phonon dispersion curve of the $KZn_{0.5}Sn_{0.5}I_3$ compound are likely due to minor numerical artifacts or insufficient *k*-point sampling and do not indicate dynamic instability. Such small negative modes are commonly encountered in complex systems and do not significantly affect the overall stability of the structure.

The frequency distribution of phonons extends from 0 to ~6.5 THz in all cases. A denser phonon spectrum is observable in $KZn_{0.5}Sn_{0.5}I_3$ (Fig. 3b) in the mid-frequency window (2–4 THz), implying stronger mode mixing and lattice complexities at the intermediate composition. Zn causes small blue shifts in some optical modes, mainly because Zn has a lower atomic mass than Sn, leading to the stiffening of Zn–I bonds. Acoustic modes show smooth and stable dispersion near the G point with an upward curvature, thus indicating that structural instabilities are absent. The Zn substitution creates many more such optical modes; consequently, coupling and splitting are more dominant in these crystals, especially for $x = 0.5$, suggesting enhanced phonon scatterings. At high-symmetry points *Q* and *Z*, phonon modes show flattening, which may affect the group velocities of vibrational modes and thus impinge upon thermal transport properties. The increased phonon mode density and dispersion complexity in $KZn_{0.5}Sn_{0.5}I_3$ lead to a reduction of lattice thermal conductivity through enhanced phonon–phonon interactions and scatterings. Such behavior would be beneficial to thermoelectric applications, for which low thermal conductivity is a virtue. The systematic shift and redistribution of vibrational modes throughout the series further suggest a tunability of vibrational entropy, thus potentially affecting phase stability and defect formation energies in Zn-doped perovskites.

3.2 Electronic properties

The electronic properties of materials play a crucial role in governing carrier transport mechanisms and in distinguishing between metals, semiconductors, and insulators. In this study, the electronic properties have been evaluated using the GGA-PBEsol[42] and HSE06 (ref. 43) functionals. A Gaussian smearing technique with a width of 0.05 eV was applied during the calculations.

3.2.1 Band structure analysis. The band gap energies are listed in Table 3. The electronic band structures of $KSn_{1-x}Zn_xI_3$ ($x = 0$, 0.25, 0.5, 0.75, and 1.0), as reported in Fig. 4, support the

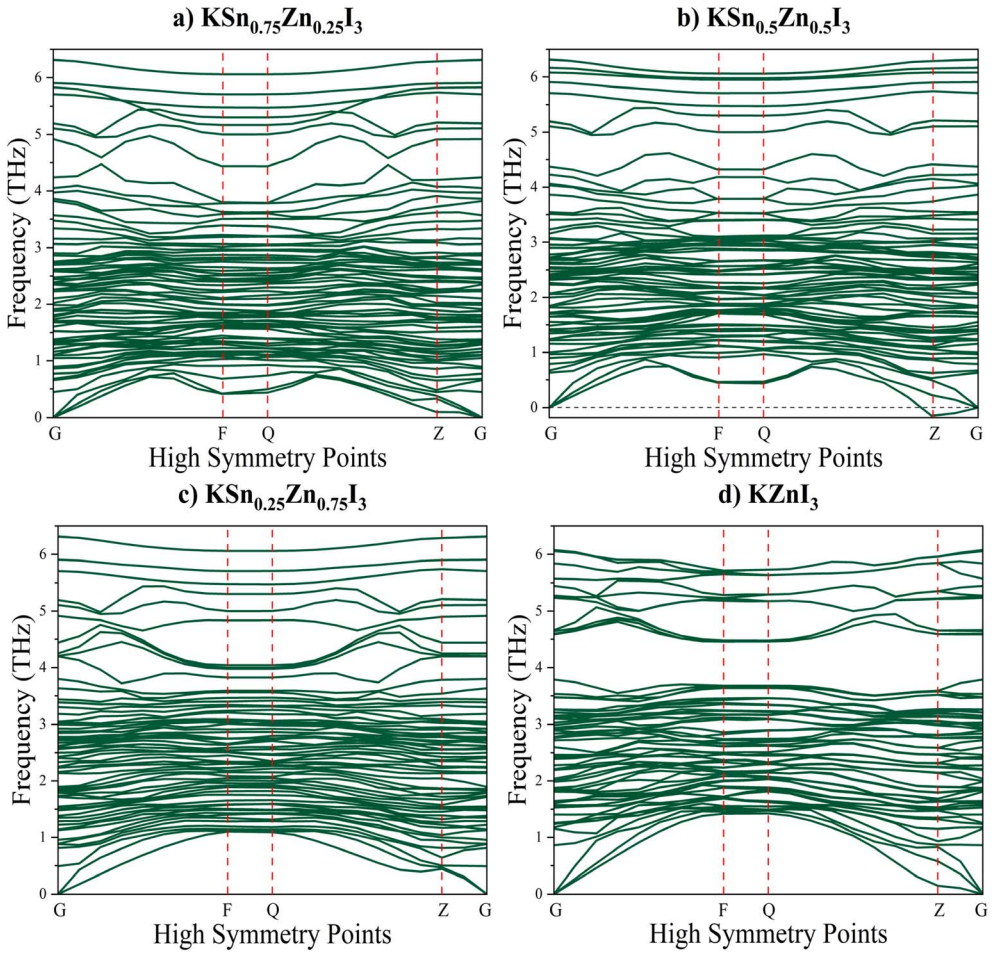

Fig. 3 Phonon dispersion curves of (a) $KSn_{0.75}Zn_{0.25}I_3$, (b) $KSn_{0.5}Zn_{0.5}I_3$, (c) $KSn_{0.25}Zn_{0.75}I_3$, and (d) $KZnI_3$ perovskite compounds.

Table 3 Calculated band gap values of $KSnI_3$, $KSn_{0.75}Zn_{0.25}I_3$, $KSn_{0.5}Zn_{0.5}I_3$, $KSn_{0.25}Zn_{0.75}I_3$, and $KZnI_3$ perovskite compounds, using the GGA-PBEsol and hybrid HSE06 functional

Compound	XC-functionals	Band gap	References
$KSnI_3$	GGA-PBEsol	1.8145 (Indirect)	This study
	GGA-PBEsol	1.84 (Indirect)	38, 49, 55, and 56
	HSE06	2.5218 (Indirect)	This study
$KSn_{0.75}Zn_{0.25}I_3$	GGA-PBEsol	1.6850 (Indirect)	This study
	HSE06	2.4838 (Indirect)	This study
$KSn_{0.5}Zn_{0.5}I_3$	GGA-PBEsol	1.8510 (Direct)	This study
	HSE06	2.6653 (Direct)	This study
$KSn_{0.25}Zn_{0.75}I_3$	GGA-PBEsol	1.4746 (Indirect)	This study
	HSE06	2.3432 (Indirect)	This study
$KZnI_3$	GGA-PBEsol	1.9579 (Indirect)	This study
	HSE06	3.0199 (Indirect)	This study

semiconducting nature for all compositions, with bandgap values varying as Zn content increases. The band gap values were initially estimated using the semi-local PBEsol exchange–correlation functional. However, it is well established that such generalized gradient approximation (GGA) functionals significantly underestimate band gaps due to self-interaction errors and the absence of non-local exchange. Therefore, the hybrid HSE06 functional, which incorporates a fraction of screened Hartree–Fock exchange, is considered more reliable and is used here for the primary discussion of electronic properties and applications. The calculated band gaps span the range 2.34–3.01 eV, placing all compositions within the wide band gap semiconductor regime. The perovskite compounds have both indirect and direct gap characteristics depending on Zn concentration.

Pristine $KSnI_3$ exhibits an indirect band gap of 2.52 eV. Although this value is too large for efficient single-junction photovoltaic absorption, it is well suited for transparent optoelectronic devices and window layers in photovoltaic devices. Such wide-band-gap materials are also relevant for tandem solar cell architectures, where selective absorption of high-energy photons is required. Beyond the band gap magnitude, the band-edge characteristics near the Fermi level provide qualitative insight into transport behavior. In particular, it has been seen that $KSnI_3$ has relatively flatter band edges, which correlate to its larger Seebeck coefficient described in the thermoelectric section.

$KSn_{0.75}Zn_{0.25}I_3$ has an indirect band gap of 2.48 eV at lower concentrations of Zn. This shows that we can achieve a modest amount of band gap tuning without significantly modifying the

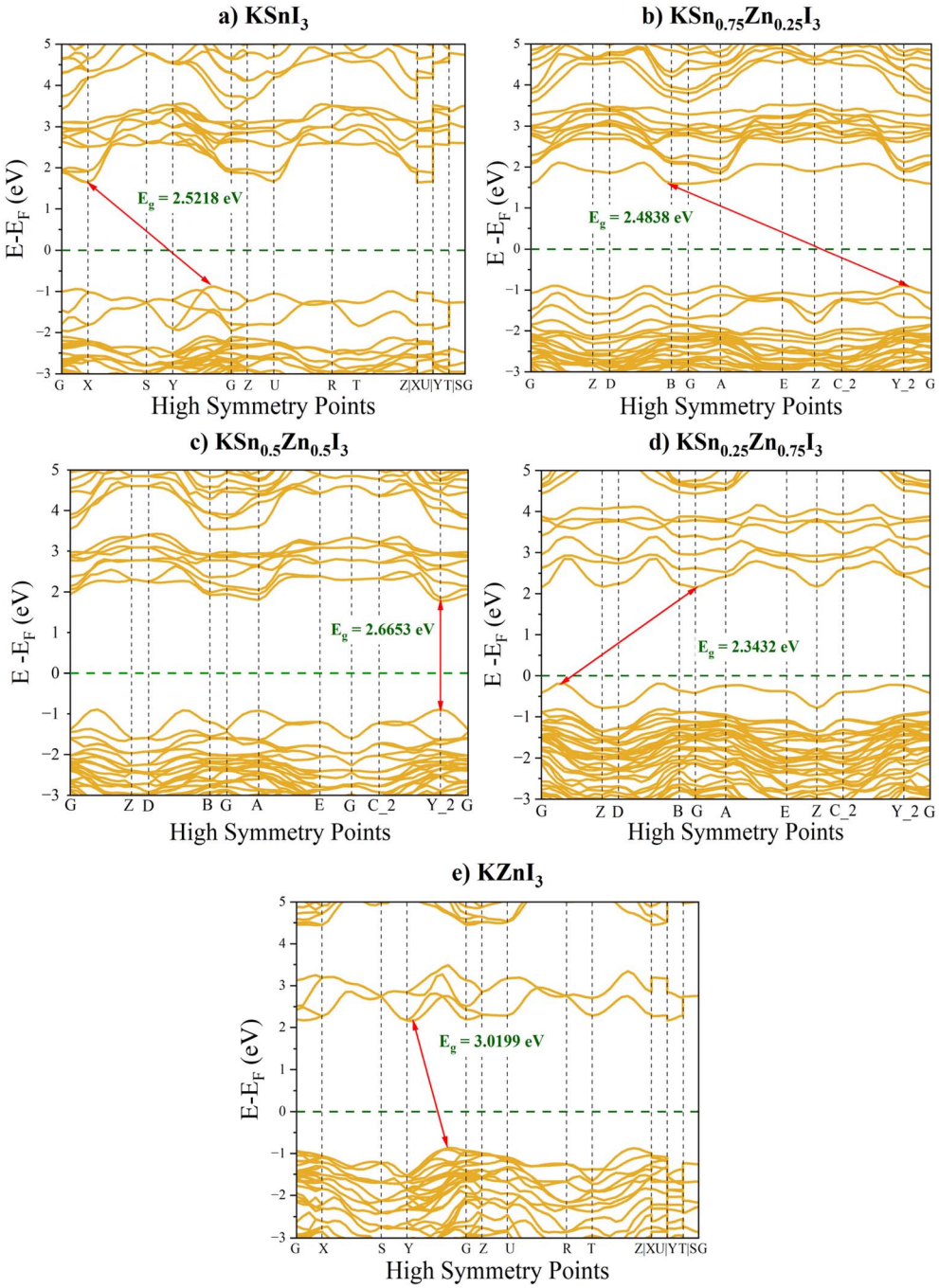

Fig. 4 Electronic band structure of (a) $KSnI_3$, (b) $KSn_{0.75}Zn_{0.25}I_3$, (c) $KSn_{0.5}Zn_{0.5}I_3$, (d) $KSn_{0.25}Zn_{0.75}I_3$, and (e) $KZnI_3$ perovskite compounds, calculated using the hybrid HSE06 functional.

overall electronic structure of the material. Although it is still not the best choice for a primary photovoltaic absorber, it would be a promising candidate for a transparent optoelectronic device and the top cell in a tandem solar cell. The indirect-to-direct band gap transition is seen within $KSn_{0.50}Zn_{0.50}I_3$, having a direct 2.67 eV band gap. The direct gap will increase the amount of radiative recombination and optical absorption, which is desirable for use in LEDs or high-speed photodetectors that are used in the visible to near ultraviolet spectral range. With further Zn incorporation, $KSn_{0.25}Zn_{0.75}I_3$ shows an indirect band gap of 2.34 eV, while fully substituted $KZnI_3$ exhibits the widest indirect band gap of 3.01 eV. These materials clearly fall within the wide-band-gap regime, supporting their potential use in UV optoelectronics, transparent electronics, and the top cell of a tandem solar cell. Moreover, the more dispersive band edges in $KZnI_3$ are consistent with its enhanced carrier mobility and electrical conductivity. This is in agreement with the thermoelectric transport results discussed in the following section.

3.2.2 Density of states analysis (DOS). The density of states (DOS) plots (Fig. 5) for the composition series $KZn_xSn_{1-x}I_3$ ($0 \leq x \leq 1$) remarkably illustrate the evolution of the electronic structure and the nature of the bandgap as Zn substitution at the Sn-site increases. For $x = 0$ (pure $KSnI_3$), the valence band maxima (VBM) are primarily composed of the I-5p orbitals, while the Sn-5p orbitals dominate the conduction band minima. This configuration results in a comparatively wide indirect bandgap, with the main quantum of energy corresponding to the asymmetric electron density of the Sn^{2+} lone pair. With a partial substitution of Sn by Zn at $x = 0.25$, the Zn-4s and Zn-4p states begin to intrude into the onset of the conduction band, signaling a transformation in the electronic structure and narrowing the band gap, although the band gap remains indirect. At an intermediate composition of Zn ($x = 0.5$), the conduction band minimum (CBM) is primarily dominated by the Zn-4s orbital rather than being heavily influenced by the Sn orbitals. This process produces a more symmetrical electronic environment and helps to convert the band gap from an indirect to a direct band gap. And, this phenomenon makes

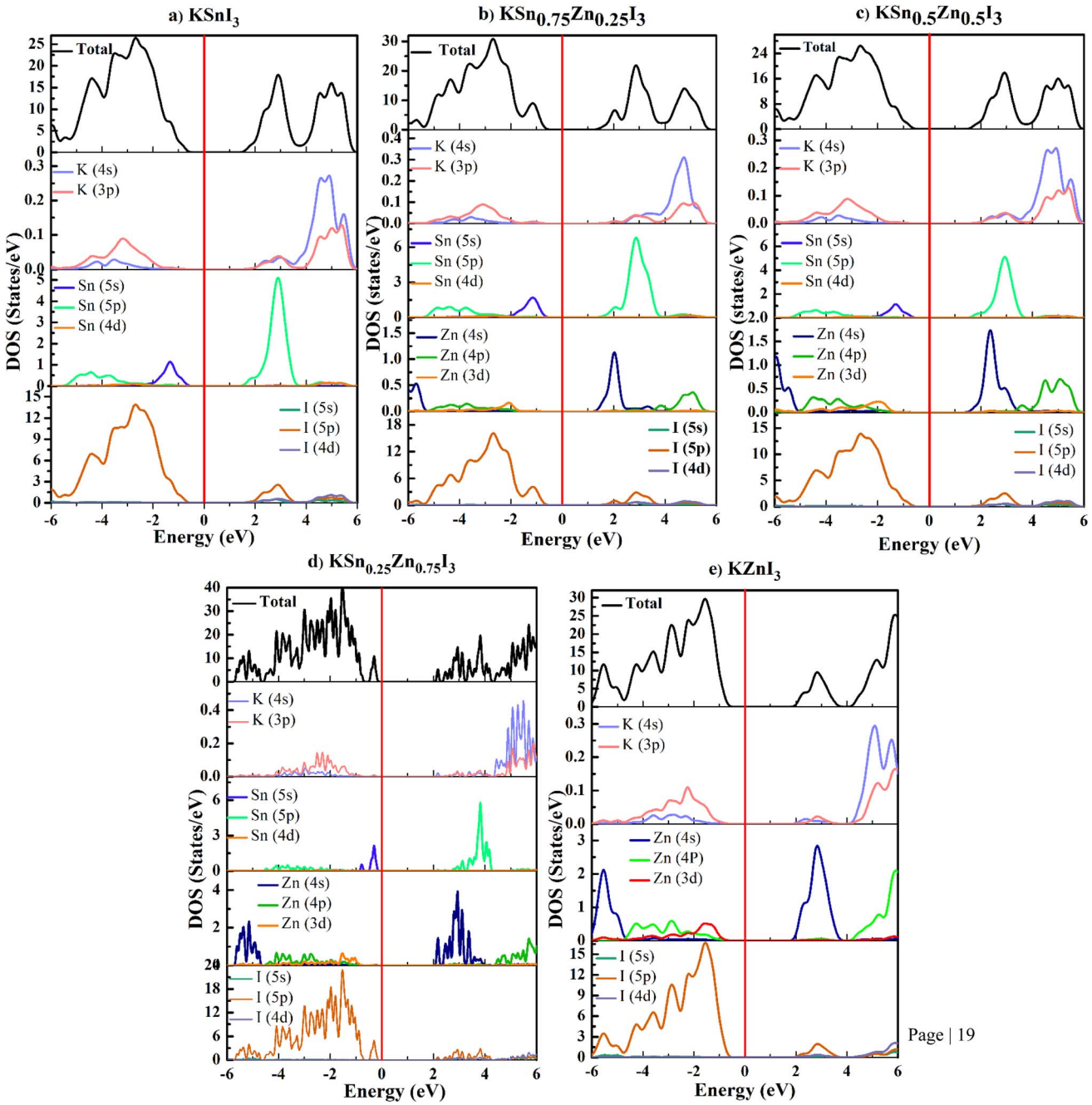

Fig. 5 The total density of states and partial density of states of (a) $KSnI_3$, (b) $KSn_{0.75}Zn_{0.25}I_3$, (c) $KSn_{0.5}Zn_{0.5}I_3$, (d) $KSn_{0.25}Zn_{0.75}I_3$, and (e) $KZnI_3$ perovskite compounds, calculated using the hybrid HSE06 functional.

the transition of electrons from valence band to the conduction band much easier upon light absorption, which is beneficial for photovoltaic applications. With further Zn substitution at $x = 0.75$ and 1.0, the CBM becomes entirely dominated by Zn orbitals. However, the VBM continues to be largely characterized by I-5p orbitals. In this situation, the hybridization between VBM and CBM states diminishes. As a result, there is a decrease in the symmetrical electronic environment, while the bandgap reverts to indirect. Thus, the DOS analysis has revealed a strong dependence of the band nature on Zn composition, with a direct bandgap developing and band gap narrowing with Zn concentrations.

From the DOS plots, it is clear that Zn-doping in $KZn_xSn_{1-x}I_3$ causes bandgap reduction, especially around $x = 0.75$, with Zn-4s and 4p states contribute significantly to the CBM. In pure $KSnI_3$ ($x = 0$), the CBM mainly consists of Sn-5p orbitals, while the VBM is dominated by I-5p states, resulting in a relatively wider bandgap. When Zn replaces Sn, particularly at concentrations ($x = 0.75$), the Zn states hybridize significantly with I-5p states at the lower-energy CBM, thereby narrowing the bandgap. Additionally, the absence of a stereochemically active Sn^{2+} $5s^2$ lone pair in Zn^{2+}, reduces local lattice distortions and promotes a better orbital alignment between VBM and CBM, producing a narrow bandgap. This behavior exemplifies how Zn substitution modifies the electronic structure and local symmetry, enabling cation engineering of tunable bandgap properties.

3.3 Optical properties

Light is a naturally abundant and renewable energy source that has high potential in optoelectronics. Currently, there is much research focused on the field of optoelectronics to develop new types of materials capable of converting light energy into electrical energy. This research focuses on parameters associated with the optical properties, such as light absorption, light reflection, refraction index, and optical conductivity of the $KZn_xSn_{1-x}I_3$ perovskites. By choosing to alloy with a specific element, researchers can easily achieve wavelength-specific tunability of optical properties such as; refraction index (n), extinction coefficient (k), reflectivity (R), energy loss function (L), dielectric constant (ε), and absorption coefficient (α).

3.3.1 Dielectric function. The dielectric function (ε) is the optical property that is consists of both the real $\varepsilon_1(\omega)$ and the imaginary $\varepsilon_2(\omega)$ components of the dielectric function. Dielectric function is the study to understand the optical interactions with solid materials.[57] The objective of this study is to analyze the dielectric function of $KZn_xSn_{1-x}I_3$ perovskite materials along with their real part $\varepsilon_1(\omega)$, and the imaginary part $\varepsilon_2(\omega)$, and the relationship of these two components for the specific perovskite materials can be obtained from the following equation,

$$\varepsilon(\omega) = \varepsilon_1(\omega) + i\varepsilon_2(\omega)$$

The real part of the dielectric function $\varepsilon_1(\omega)$ describes the polarization response of materials to an applied electric field and the propagation of electromagnetic waves within the material. And, the imaginary component of the dielectric function describes how much energy is absorbed by that same material. In terms of perovskite solar cells, the imaginary part is particularly significant because it explains the mechanisms by which these types of solar cells convert electromagnetic wave energy into electrical energy.[57]

Fig. 6(a) illustrates how the value of dielectric function $\varepsilon_1(\omega)$ varies for $KZn_xSn_{1-x}I_3$ perovskites in the range of 0–10 eV. The static dielectric constant $\varepsilon_1(0)$, which is the value at 0 eV of the real part of the dielectric function.[58] As shown in Fig. 6(a), $KSnI_3$ (5.86) has the largest real value of the dielectric function at 0 eV as compared to other Zn-doped compounds and the $KZnI_3$ (4.93) has the least value. Therefore, the addition of Zn in the $KSn_{1-x}Zn_xI_3$ material appears to cause a downward trend in the static dielectric constant and charge storage capacity. The decline of charge storage capacity is much less substantial than that of the original $KSnI_3$ material, and so the doped materials are still appropriate for use in optoelectronic devices.

The imaginary component $\varepsilon_2(\omega)$ of the dielectric function of a material is a measure of its capacity to absorb light. Electronic transitions between valence and conduction band states determine the value of $\varepsilon_2(\omega)$. The peaks of the $\varepsilon_2(\omega)$ curve correspond to these transitions and indicate the energy gaps associated with them.[59] As illustrated in Fig. 6(b), an increase in $\varepsilon_2(\omega)$ occurs at the point where the energy of the incoming photons exceeds the material's bandgap. For $KZn_xSn_{1-x}I_3$, the value of $\varepsilon_2(\omega)$ remains close to zero until the incident energy threshold is reached. Once this threshold has been crossed, $\varepsilon_2(\omega)$ rises quickly and achieves maximum values of 9.63 $KSnI_3$, 9.62 $KZnI_3$, 7.97 $KSn_{0.75}Zn_{0.25}I_3$, 6.61 $KSn_{0.5}Zn_{0.5}I_3$, and 7.20 for $KSn_{0.25}Zn_{0.75}I_3$ Perovskite compounds.

3.3.2 Absorption coefficient. Absorption coefficient ($\alpha(\omega)$) provides a measurement of the amount of light (photons) at a given wavelength that can be absorbed by materials as they pass through that material. As one of the most important optical properties of a material, the absorption coefficient typically determines how effectively photons are absorbed by the material. The absorption spectrum will typically be used to determine a material's ability to function in photovoltaic applications.[60] The following equation can be used to calculate the absorption coefficient $\alpha(\omega)$ of any given material.[61]

$$\alpha(\omega) = \left[\sqrt{\varepsilon_1{}^2(w) + \varepsilon_2{}^2(w)} - \varepsilon_2(w)\right]_{1/2}$$

Fig. 6(c) shows the optical absorption coefficients of all the pristine and alloyed perovskite compositions: $KSnI_3$, $KSn_{0.25}Zn_{0.75}I_3$, $KSn_{0.5}Zn_{0.5}I_3$, $KSn_{0.75}Zn_{0.25}I_3$, and $KZnI_3$. All compounds have strong UV and visible absorbance (200–600 nm) across the entire wavelength, which is an important characteristic for efficient optoelectronic operation.[62] Except for the $KSn_{0.75}Zn_{0.25}I_3$, the overall trend suggests that a slight increase in Zn content reduces optical absorption compared to pure $KSnI_3$. The $KSn_{0.75}Zn_{0.25}I_3$ exhibits relatively high absorption (8.15×10^5 cm^{-1}), particularly at shorter wavelengths (UV-region), reflecting a strong light-matter interaction (Fig. 6(c)).

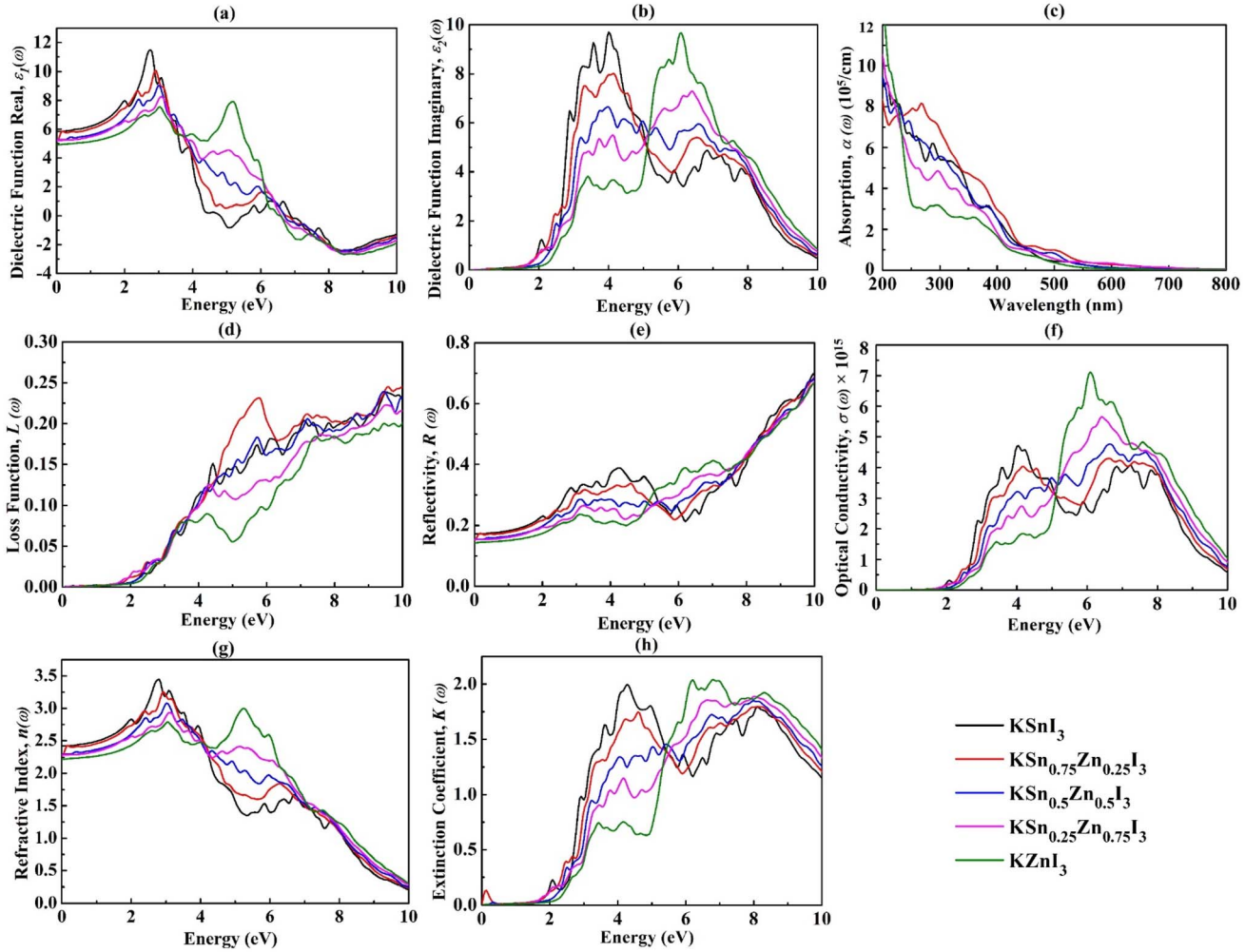

Fig. 6 The optical properties of the studied $KSn_{1-x}Zn_xI_3$ perovskite compounds calculated with the HSE06 hybrid functional: (a) real part of the dielectric constant ($\varepsilon_1(\omega)$), (b) imaginary part of the dielectric constant ($\varepsilon_1(\omega)$), (c) absorption coefficient ($\alpha(\omega)$), (d) energy loss function ($L(\omega)$), (e) reflectivity ($R(\omega)$), (f) optical conductivity ($\sigma(\omega)$), (g) refractive index ($n(\omega)$), and (h) extinction coefficient ($K(\omega)$).

This compound also exhibits a reduced band gap of 2.48 eV compared to 2.52 eV for pure $KSnI_3$, suggesting promising potential for UV-photodetectors, blue-light LEDs, top cells in tandem solar cells, and photocatalytic systems that operate in the higher-energy spectrum. However, as Sn is gradually replaced by Zn (from $KSn_{0.50}Zn_{0.50}I_3$ to $KZnI_3$), there is a clear decline in absorption intensity. However, the pure $KZnI_3$ shows the lowest absorption (3.15×10^5 cm^{-1}) and highest bandgap (3.01 eV) among all, suggesting that only partial substitution of Zn ($KSn_{0.25}Zn_{0.75}I_3$) plays an important role in boosting the light absorption capacity of these materials and broadens the range of usable light due to the band gap reduction.[58]

3.3.3 Loss function. The loss function ($L(\omega)$) represents the energy lost by high-speed electrons as they pass through a material, capturing important interactions like interband transitions, intraband excitations, and plasmon resonances. This function shows how fast-moving charged particles, in this case electrons, interact with the materials.[63] As shown in Fig. 6(d), the doped compositions with Zn, especially $KSn_{0.75}Zn_{0.25}I_3$, have the greatest value of electron energy loss function (0.23) at 5.75 eV. Thus, they have the highest probability of interacting with the fast-moving electron. Also, the $KSnI_3$ (0.16) and $KSn_{0.25}Zn_{0.75}I_3$ (0.12) all demonstrate intermediate levels of energy loss and thus interact with the fast-moving electrons. The lowest level of energy loss function occurred with the $KZnI_3$ (0.091) because of the reason of having the largest band gap.

3.3.4 Optical reflectivity. Optical reflectivity ($R(\omega)$) refers to the percentage of the incoming light that is reflected off the surface of a material. This value is very important in determining how light interacts with solids and will assist in the design of materials for use as photovoltaic materials. The reflective characteristics of any material can be determined through the given equation.[61]

$$R(\omega) = \frac{(1-n)^2 + k^2}{(1+n)^2 + k^2}$$

The best absorbing material for solar cells should have low reflectance in the visible and near infrared range (300–1100 nm

or 1–4 eV) in order to ensure maximum photon absorption and conversion into electricity.[62] Fig. 6(e) shows how the reflectance $R(\omega)$ of various perovskite compounds changes at different photon energy. The $KSnI_3$ has the highest reflectance value of 37%, thus it reflects more sunlight than other types of perovskite compositions. In contrast, the $KZnI_3$ exhibits a low reflectance value of 0.21, making it one of the least reflective perovskites, especially within the visible to near Infrared portion. Essentially, lowering the reflectance of a perovskite material by doping with Zn allows for a higher absorbance of incoming solar energy. Therefore, having lower reflectance in perovskite materials will save on energy while providing better quality products from a manufacturing standpoint.

3.3.5 Optical conductivity. A graphical comparison of the optical conductivity ($\sigma(\omega)$) for several different perovskite materials is plotted with respect to photon energy (eV) in Fig. 6(f). Optical conductivity gives an indication of how well each perovskite can conduct electricity when exposed to light.[64] The optical conductivity of a material is defined by the following equation.[61]

$$\sigma(\omega) = -\frac{i\omega}{4\pi}\varepsilon(\omega)$$

At photon energies below 2 eV, all perovskites exhibit nearly zero optical conductivity. This occurs because photons with an energy lower than the bandgap energy do not provide enough energy to promote potentially conductive electrons from the valence band into the conduction band. After 2 eV, there is a sharp increase in conductivity because there is now enough energy in the incident photons to excite electrons into the conduction band. It is observed that above 6 eV, there is very strong optical conductivities, which gives $KSn_{1-x}Zn_xI_3$ perovskites huge potential for applications in UV-sensitive optoelectronics. In this case, $KZnI_3$ has the highest conductivity due to its relatively high bandgap (3.01 eV), which suggests strong photoconductivity driven by the UV-range photon shining on the material.

3.3.6 Refractive index and extinction coefficient. The refractive index ($n(\omega)$) measures how much light bends, or changes direction, when it passes from one material into another.[65] The formulas used to calculate the refractive index and extinction coefficient are;

$$n(\omega) = \frac{1}{\sqrt{2}}\left(\sqrt{\varepsilon_1(\omega)^2 + \varepsilon_2(\omega)^2} + \varepsilon_1(\omega)^{\frac{1}{2}}\right)$$

$$k(\omega) = \frac{1}{\sqrt{2}}\left(\sqrt{\varepsilon_1(\omega)^2 + \varepsilon_2(\omega)^2} - \varepsilon_1(\omega)^{\frac{1}{2}}\right)$$

As can be seen in Fig. 6(g), with the increase of Zn-doping in $KSn_{1-x}Zn_xI_3$ perovskite compounds, the static refractive index $n(0)$ decreases and continues decreasing as the resulting amount of Zn-doping increases. The static refractive index of $KSnI_3$, $KSn_{0.75}Zn_{0.25}I_3$, $KSn_{0.25}Zn_{0.75}I_3$, $KSn_{0.5}Zn_{0.5}I_3$, and $KZnI_3$ is 2.41, 2.33, 2.29, 2.29, and 2.20, respectively. Thus, Zn doping will cause perovskites to bend light less effectively, resulting in slightly reduced photon trapping in thin films. This can be considered an unfavorable characteristic for the design of layered tandem solar cells with $KSn_{1-x}Zn_xI_3$ perovskite compounds. However, this potential disadvantage can be minimized where the layered tandem solar cell layout uses a combination of anti-reflective coatings and light-trapping structures.

The extinction coefficient ($k(\omega)$) of the $KSn_{1-x}Zn_xI_3$ compound is displayed in Fig. 6(h) over the energy range up to 10 eV. Initially, the extinction coefficient values remained almost zero up to 2 eV. Beyond this point, it increased gradually with increasing energy, corresponding to the onset of strong interband electronic transitions from the valence band to the conduction band. Pristine $KSnI_3$ exhibits pronounced extinction features in the visible and near-ultraviolet regions, with a major peak around 4–5 eV, followed by additional high-energy peaks extending up to ~8 eV. The fully substituted $KZnI_3$ compound shows a comparatively weaker extinction coefficient in the lower-energy region but displays strong extinction in the higher-energy range (~5–8 eV), reaching the largest peak intensity among all compositions. This behavior suggests enhanced optical transitions in the ultraviolet region for Zn-rich compositions. Fig. 6(h) also indicates that the gradual substitution of Sn with Zn in the perovskite structure leads to a decrease in extinction coefficients up to 5.44 eV photon energy, and after that, the trend becomes opposite. The impact of Zn doping on the evolution of $k(\omega)$ supports that alloying is an excellent means of modifying both the optical extinction coefficient and the spectral properties of $KSn_{1-x}Zn_xI_3$ perovskite compounds.

3.4 Thermo-mechanical properties

A complete comprehension of the internal structure of solid material is associated with elastic constants, which ensure the structural stability of the material. Elastic properties play a crucial role in material science, as they allow materials to spring back to their original shape after facing external forces.[49] In this study, independent elastic constants are first evaluated using strain–stress calculations, which served as the basis for the investigation of mechanical properties.[66] To find the mechanical behavior and structural stability of the $KSn_{1-x}Zn_xI_3$ perovskite series, key elastic parameters such as bulk modulus (B), Young's modulus (Y), shear modulus (G), and Poisson's ratio (ν) are calculated. The mechanical properties of Zn-doped $KSn_{1-x}Zn_xI_3$ perovskites with orthorhombic and monoclinic crystal structures are calculated with the GGA-PBEsol functional. The values of calculated elastic constants C_{ij} for $KSn_{1-x}Zn_xI_3$ perovskites are provided in Table 4. Among different compositions of $KSn_{1-x}Zn_xI_3$; the $KSnI_3$ and $KZnI_3$ have an orthorhombic crystal structure, while the partially Zn-substituted compounds $KSn_{0.75}Zn_{0.25}I_3$, $KSn_{0.5}Zn_{0.5}I_3$, and $KSn_{0.25}Zn_{0.75}I_3$ have a monoclinic structure. The conditions for mechanical stability depend on the type of crystal structure, where orthorhombic and

Table 4 The computed elastic constants C_{ij} (Gpa) for $KSn_{1-x}Zn_xI_3$ (x = 0, 0.25, 0.50, 0.75, 1) perovskite compositions

Compound	C_{11}	C_{12}	C_{13}	C_{15}	C_{22}	C_{23}	C_{25}	C_{33}	C_{35}	C_{44}	C_{46}	C_{55}	C_{66}
$KSnI_3$ (ref. 49)	26.40	12.46	11.01	—	15.22	13.50	—	24.51	—	5.98	—	7.74	11.67
$KSnI_3$	18.52	16.02	15.39	—	30.12	13.10	—	33.31	—	8.29	—	5.93	14.02
$KSn_{0.75}Zn_{0.25}I_3$	16.87	9.73	10.98	−0.18	21.49	10.30	−1.06	21.27	−0.42	3.66	0.26	3.88	11.90
$KSn_{0.50}Zn_{0.50}I_3$	24.38	13.92	16.10	3.16	25.45	14.88	2.55	35.15	−0.33	10.30	3.08	5.37	8.241
$KSn_{0.25}Zn_{0.75}I_3$	30.72	15.56	16.08	4.18	37.69	16.51	3.43	29.45	2.34	10.78	1.57	6.74	10.89
$KZnI_3$	34.05	17.05	18.55	—	36.71	18.99	—	37.07	—	12.80	—	8.67	11.65

monoclinic crystals each have their own specific elastic stability requirements. The mechanical stability criteria for the orthorhombic crystal structure are;[67]

$$C_{11} > 0,\ C_{44} > 0,\ C_{55} > 0,\ C_{66} > 0,\ (C_{11} \times C_{12}) > {C_{12}}^2,$$

and

$$(C_{11} \times C_{22} \times C_{33}) + 2(C_{12} \times C_{13} \times C_{23}) - (C_{11} \times {C_{23}}^2) - (C_{22} \times {C_{13}}^2) - (C_{33} \times {C_{12}}^2) > 0$$

The mechanical stability criteria for the monoclinic crystal system are;[67]

$$C_{11} > 0,\ C_{22} > 0,\ C_{33} > 0,\ C_{44} > 0,\ C_{55} > 0,\ C_{66} > 0,$$

$$[C_{11} + C_{22} + C_{33} + 2(C_{12} + C_{13} + C_{23})] > 0,$$

$$[(C_{33} \times C_{55}) - {C_{35}}^2 > 0,\ (C_{44} \times C_{66}) - {C_{46}}^2 > 0,\ (C_{22} + C_{33} - 2C_{23})] > 0,$$

$$[C_{22}(C_{33} \times C_{55} - {C_{35}}^2) + 2(C_{23} \times C_{25} \times C_{35}) - ({C_{23}}^2 \times C_{55}) - ({C_{25}}^2 \times C_{33})] > 0,$$

and

$$2[C_{15} \times C_{25}(C_{33} \times C_{12} - C_{13} \times C_{23}) + C_{15} \times C_{35}(C_{22} \times C_{13} - C_{12} \times C_{23}) + C_{25} \times C_{35}(C_{11} \times C_{23} - C_{12} \times C_{13})] - [C_{15} \times C_{15}(C_{22} \times C_{33} - {C_{23}}^2) + C_{25} \times C_{25}(C_{11} \times C_{33} - {C_{13}}^2) + C_{35} \times C_{35}(C_{11} \times C_{22} - {C_{12}}^2)] + C_{55} \times g > 0$$

It is observed that conditions mentioned in the above equations are satisfied for all $KSn_{1-x}Zn_xI_3$ perovskite compositions. Therefore, all the perovskite compositions are mechanically stable perovskite compounds.

By using the elastic constants provided in Table 4, the bulk and shear modulus are calculated with the Ruess (B_R, G_R) and Voigt approximation.[68,69] The Hill approximation's bulk modulus (B_H) and shear modulus (G_H) are determined by taking the arithmetic mean of the values obtained from the Ruess and Voigt approximations.[70] This approach provides a more accurate estimation of the overall mechanical properties by averaging the extremes of elastic responses. The values of the bulk and shear modulus of all the $KSn_{1-x}Zn_xI_3$ perovskite compositions are provided in Table 5. Table 5 and Fig. 7 indicate that the gradual substitution of Sn with Zn in the perovskite structure leads to a change in mechanical properties. While an initial reduction in bulk, shear, and Young's moduli is observed at low Zn content (x = 0.25), further increase is observed in these properties with increasing Zn concentration in the perovskite structure, which indicates enhanced mechanical stability and stiffness. The smaller ionic radius and stronger bonding characteristics of the Zn-ions compared to the Sn-ions contribute to a more compact and rigid crystal lattice.

The Pugh's ratio (B/G) measures whether a material will break easily (brittle) or deform before breaking, by comparing its stiffness to its resistance to shear.[71] According to the B/G ratio criterion, materials with a B/G value greater than 1.75 are considered ductile, while those with a value less than 1.75 are classified as brittle. Similarly, another important elastic behavior, which also helps distinguish between brittle and ductile behavior, is Poisson's ratio (ν). According to Frantsevich's rule, materials with a Poisson's ratio greater than 0.26 (ν > 0.26) are considered ductile, while those with values below this threshold are classified as brittle.[8] As evident from Table 5, all the investigated compounds of $KSn_{1-x}Zn_xI_3$ exhibit Poisson's ratio values ranging from 0.316 to 0.335 and B/G ratio ranging from 2.39 to 2.70 (Fig. 7(b), and Table 5). This indicates that all the studied compounds, $KSnI_3$, $KSn_{0.75}Zn_{0.25}I_3$, $KSn_{0.5}Zn_{0.5}I_3$, $KSn_{0.25}Zn_{0.75}I_3$, and $KZnI_3$, are ductile and excellent for fabricating thin films on flexible substrates.

The universal anisotropy factor (A^U) and its variation with different Zn-doping concentrations in $KSn_{1-x}Zn_xI_3$ perovskite compositions are presented in Table 5 and illustrated in Fig. 7(b). The completely elastic isotropic material has an A^U value equal to zero. On the contrary, the A^U value of an anisotropic material deviates from zero.[58] All the compositions of Zn-doped $KSn_{1-x}Zn_xI_3$ perovskites exhibit an anisotropic nature, as the A^U value differs from zero (Fig. 7(b), and Table 5). However, with increasing Zn concentration, the A^U values progressively approach zero, indicating a gradual transition toward elastic isotropy induced by Zn incorporation. In particular, the perovskite compositions $KSn_{0.25}Zn_{0.75}I_3$ and $KZnI_3$ have A^U values very close to zero, which indicates the nearly isotropic nature of these compositions. Therefore, the Zn-doped compositions are less prone to micro-crack formation after fabrication compared to pristine $KSnI_3$ perovskite.

Table 6 summarizes the calculated density (ρ), longitudinal (ν_l), transverse (ν_t), and average sound velocities (ν_m), Debye temperature (Θ_D), and melting temperature (T_m) of $KSn_{1-x}Zn_xI_3$ (x = 0, 0.25, 0.50, 0.75, and 1) perovskite compounds. These

Table 5 Calculated elastic properties of $KSn_{1-x}Zn_xI_3$ compounds, including the bulk modulus B (GPa), Young's modulus Y (GPa), shear modulus G (GPa), Poisson's ratio (ν), Pugh's ratio (B/G), and universal elastic anisotropy factor (A^U)

Compound	B_V	G_V	B_R	G_R	B_H	G_H	E	ν	B/G	A^U
$KSnI_3$ (ref. 49)	15.57	7.02	14.54	5.21	15.05	6.11	16.16	0.321	2.46	—
$KSnI_3$	19.00	8.14	17.69	6.15	18.35	7.15	18.98	0.328	2.57	1.69
$KSn_{0.75}Zn_{0.25}I_3$	13.52	5.80	13.26	4.72	13.39	5.26	13.95	0.326	2.55	1.16
$KSn_{0.50}Zn_{0.50}I_3$	19.42	7.46	17.65	6.29	18.53	6.87	18.35	0.335	2.70	1.03
$KSn_{0.25}Zn_{0.75}I_3$	21.57	8.99	19.72	8.28	20.64	8.64	22.74	0.316	2.39	0.53
$KZnI_3$	24.11	10.17	24.03	9.89	24.07	10.03	26.43	0.317	2.40	0.15

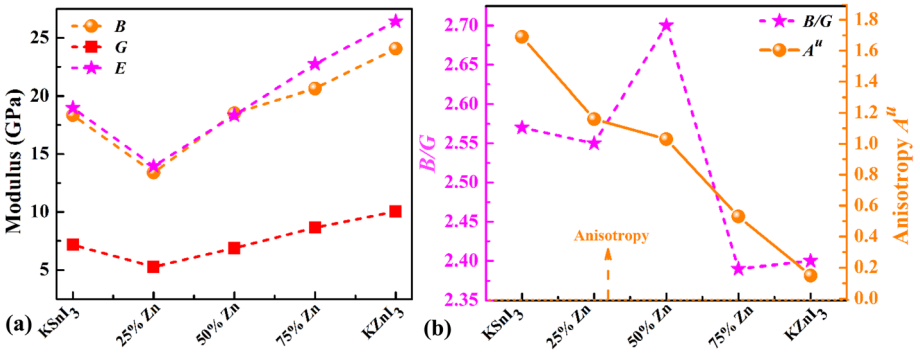

Fig. 7 Mechanical properties variation of $KSn_{1-x}Zn_xI_3$ (x = 0, 0.25, 0.50, 0.75, and 1) perovskites due to Zn doping; (a) elastic modulus (E), shear modulus (G), and bulk modulus (B), and (b) Pugh's ratio (B/G), and universal elastic anisotropy factor (A^U).

parameters play a crucial role in determining the lattice thermal conductivity and thermal stability, which are key factors for thermoelectric performance. The progressive substitution of Sn by Zn leads to a monotonic increase in density, indicating enhanced lattice rigidity and improved thermal stability with increasing Zn concentration. The formulas for the melting temperature of orthorhombic and monoclinic crystals are expressed as;[64]

$$T_m = 412 + 8.2\,[C_{11} + {C_{12}}^{1.25}]$$

$$T_m = 412 + 8.2\left[\frac{C_{11} + C_{22} + C_{33}}{3} + {C_{12}}^{1.25}\right]$$

The increase in melting point with the addition of Zn from 835 K ($KSnI_3$) to 980 K ($KZnI_3$) suggests enhanced interatomic bonding from the incorporation of Zn. Thus, the Zn-doped compounds are suitable for high-temperature thermoelectric applications because of increased thermal stability. With Zn content, the average sound velocity and the Debye temperature vary non-monotonically. The $KSn_{0.75}Zn_{0.25}I_3$ exhibits the lowest average sound velocity of 1257 m s^{-1} and the lowest Debye temperature of 108 K. This behavior suggests that the lattice thermal conductivity will be reduced due to the direct relation between lattice thermal conductivity, phonon group velocity, and Debye temperature. Low lattice thermal conductivities greatly improve the thermoelectric figure of merit, and this behavior makes them favorable to use in thermoelectric applications. As the concentration of Zn increases, both the value of ν_m and Θ_D rise to their maximum values for $KZnI_3$ composition. This is due to stronger bonding between the atoms and higher velocities of phonons within the structure, leading to improved overall thermal stability of the material. However, while compositions with Zn provide greater thermal stability, intermediate alloyed compositions should yield the best balance

Table 6 Calculated thermal properties of $KSn_{1-x}Zn_xI_3$ compounds, including density (ρ), longitudinal (ν_l), transverse (ν_t), and average sound velocities (ν_m), Debye temperature (Θ_D), and melting temperature (T_m)

Compound	ρ (kg m^{-3})	ν_l (m s^{-1})	ν_t (m s^{-1})	ν_m (m s^{-1})	Θ_D (K)	T_m (K)
$KSnI_3$	4280	2482	1257	1409	123	835
$KSn_{0.75}Zn_{0.25}I_3$	4590	2210	1122	1257	108	845
$KSn_{0.5}Zn_{0.5}I_3$	4620	2447	1219	1367	123	915
$KSn_{0.25}Zn_{0.75}I_3$	4705	2614	1355	1516	138	950
$KZnI_3$	4814	2790	1444	1617	149	980

between reducing the thermal conductivity of the lattice and maintaining structural integrity.

Overall, the decrease in Debye temperature and sound velocities observed in the partially substituted zinc compositions provides evidence that the phonon transport is impeded due to alloy scattering arising from Sn/Zn disorder. Together, the softening mechanism of phonons and the sufficient range of melting temperatures indicate that $KZnI_3$ is a potential candidate for future thermoelectric device applications. However, further investigation into the electrical transport properties will be necessary before establishing conclusively whether or not $KZnI_3$ is suitable for use in thermoelectric devices.

Together, the computed melting temperatures, negative formation energies, and phonon stability show that $KSn_{1-x}Zn_xI_3$ compounds are suitable for high-temperature thermoelectric applications because they have good intrinsic structural robustness. Nevertheless, the current calculations do not specifically account for finite-temperature effects like thermal expansion or temperature-driven phase transitions because they are based on the optimized ground-state structures. At high temperatures, these effects could affect electronic transport, lattice thermal conductivity, and phonon scattering. Future research should focus on a more thorough evaluation of high-temperature structural evolution using *ab initio* molecular dynamics or quasi-harmonic calculations.

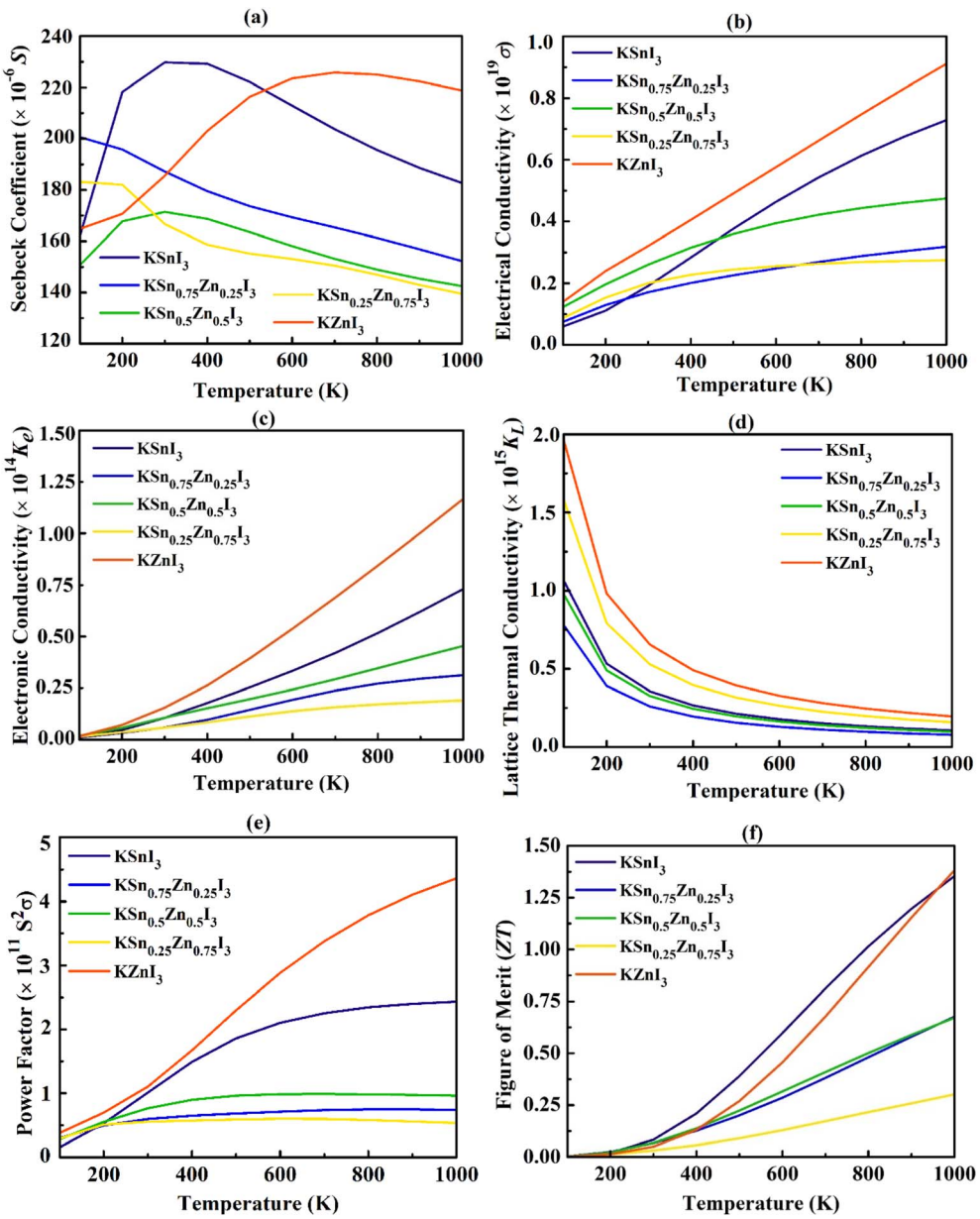

Fig. 8 Temperature-dependent thermoelectric properties of $KSn_{1-x}Zn_xI_3$ compounds (x = 0, 0.25, 0.5, 0.75, and 1): (a) Seebeck coefficient (S), (b) electrical conductivity (σ), (c) electronic conductivity (K_e), (d) lattice thermal conductivity (K_L), (e) power factor (PF), and (f) figure of merit (ZT).

3.5 Thermoelectric properties

The graphs in Fig. 8 illustrate how the temperature affects each of the following variables: (a) Seebeck coefficient (S), (b) electrical conductivity (σ), (c) electronic conductivity (K_e), (d) lattice thermal conductivity (K_L), (e) power factor ($S^2\sigma$), and (f) thermoelectric figure of merit (ZT). The thermoelectric effect allows the direct conversion of a temperature difference into an electrical voltage and *vice versa*. The efficiency of a thermoelectric material is quantified by the dimensionless figure of merit, ZT,[72] given by:

$$ZT = \frac{S^2\sigma}{K}T$$

Here, S is the Seebeck coefficient, σ is the electrical conductivity, K is the total thermal conductivity (the sum of electronic (K_e) and lattice (K_L) contributions), and T is the absolute temperature. An optimal thermoelectric material requires a high-power factor (PF = $S^2\sigma$) coupled with a low thermal conductivity (K).

In this study, key transport coefficients, including the Seebeck coefficient (S), electrical conductivity (σ), and electronic thermal conductivity (K_e) are calculated using the semi-classical Boltzmann transport theory within the constant relaxation time approximation (CRTA). Carrier concentration within the CRTA framework was utilized to compare intrinsic-temperature and composition-dependent trends across the $KSn_{1-x}Zn_xI_3$ series. This approximation assumes the electron relaxation time (τ) is energy-independent. This is a standard approach when precise τ calculations from first principles are computationally prohibitive. A constant τ value on the order of 10^{-14} s and a typical carrier concentration of 1×10^{20} cm^{-3} for semiconducting thermoelectric materials are employed. The assumption that is being made is consistent from current literature of DFT on similar materials. Calculations are completed using the BoltzTraP2 software,[46] and lattice thermal conductivity (K_L) is calculated using Slack's model.[73]

$$K_L = A(\gamma)\frac{M_{av}{\theta_D}^3\delta}{\gamma^2 n^{2/3}T}$$

$$\gamma = \frac{3(1+\vartheta)}{2(2-3\vartheta)}$$

$$A(\gamma) = \frac{4.85628 \times 10^7}{2\left(1 - \frac{0.514}{\gamma} + \frac{0.228}{\gamma^2}\right)}$$

Here, the symbol γ denotes the Grüneisen parameter, a measure of the anharmonicity of a phonon. A reduction in phonon thermal conductivity at high γ values indicates the presence of significant anharmonic contributions to heat conduction. The $A(\gamma)$ is a dimensionless function of the Gruneisen constant, M_{av} refers to the mean mass per molecule, θ_D is the Debye temperature, δ is the average distance between atoms, n is the number of atoms within one primitive unit cell, and T is the absolute temperature (in K). The impact of anharmonic phonon scattering and phonon group velocity on lattice heat transport is captured by the model. Thus, it is anticipated that compositions with lower average sound velocity and θ_D will have lower lattice thermal conductivity, which is in line with the trends found in this work. The dependence of the thermoelectric coefficient upon temperature is shown in Fig. 8. A complete evaluation of the thermoelectric power factor ($S^2\sigma$), total thermal conductivity (K), and resulting figure of merit (ZT) will provide insight into the thermoelectric potential of $KSn_{1-x}Zn_xI_3$ (x = 0,0.25,0.50,0.75, and 1) perovskite compounds.

3.5.1 Seebeck coefficient (S). The Seebeck coefficient *vs.* temperature variations for all compositions are shown in Fig. 8(a). Electrical conductivity as well as the Seebeck coefficient are influenced by how dispersed the band structure is near the Fermi level.[74] Also, the Seebeck coefficient has strong composition dependence and is a clear method of distinguishing the two pure compounds $KSnI_3$ and $KZnI_3$ from any intermediate alloys.

The Seebeck coefficient for $KSnI_3$ is at its maximum value of 220–230 μV K^1 at low temperature region ($100 \leq T \leq 300$ K). The reason that $KSnI_3$ has such a high Seebeck coefficient is that it has a steep band curvature and the effective mass at the Fermi level is relatively large. As the temperature increases, $KSnI_3$ shows a monotonic decrease in S value due to significant bipolar excitation typical for semiconductors. Conversely, $KZnI_3$ shows a monotonic increase in S value as the temperature increases and surpasses all the other compositions at around 650 K with S value of 225 μV K^1. The Seebeck coefficient of $KZnI_3$ is maximized at the high temperature region with increased thermal excitation of the carriers, providing a more suitable band gap for thermoelectric operation at elevated temperatures. This makes $KZnI_3$ a superior high-temperature thermoelectric material compared to compositions like $KSnI_3$.

For a clearer assessment of performance, these results can be compared with the Seebeck coefficient (S) of well-known thermoelectric compounds found in the literature. For instance, polycrystalline tin selenide (SnSe) reaches the maximum Seebeck coefficient (S) value of 668 μV K^{-1} at 380 K.[75] For the silicon-alloyed $Bi_{0.4}Sb1.6Te_3$ compounds, the Seebeck coefficient (S) value peaks at approximately 400 K, reaching values near 230 μV K^{-1}.[76] The n-type doped $CsSnI_3$ and $CsGeI_3$ perovskites exhibit Seebeck coefficient values of −300 and −280 μV K^{-1}, respectively, at 700 K.[77] In contrast, $CsPbI_3$ perovskite exhibits a low value of the Seebeck coefficient of 150 μV K^{-1} at the same temperature.[78] Among organic–inorganic mixed halide perovskites, the $MAPbI_3$ single crystal displays a very high Seebeck coefficient of almost 1693 μV K^{-1} at 351 K.[79] However, the low electrical conductivity of $MAPbI_3$ makes the ZT value very small, approximately ∼0.1–0.9.[80] Compared to these well-known thermoelectric compounds, the Seebeck coefficients of $KSnI_3$ and $KZnI_3$ fall within a competitive range along with the earth abundance of K compared to Se, Te, and Cs. This highlights their potential for further thermoelectric development.

The mixed alloys ($x = 0.25, 0.5, 0.75$) display noticeably lower Seebeck coefficients across all temperatures. This reduction occurs because alloying introduces structural changes,

chemical disorder, and lattice scattering, which alter carrier concentration and reduce carrier mobility. These effects weaken the Seebeck coefficient compared to the well-ordered pure end compounds. Thus, $KSnI_3$ dominates at low temperatures, while $KZnI_3$ has the superior high-temperature Seebeck coefficient, making the two end-members the most promising thermoelectric compounds.

3.5.2 Electrical conductivity (σ). Fig. 8(b) presents the electrical conductivity (σ) as a function of temperature (K) for five different compositions in the $KSn_{1-x}Zn_xI_3$ system. The two pure end-members, $KZnI_3$ and $KSnI_3$, exhibit the highest electrical conductivity across the entire temperature range. The electrical conductivity reaches approximately 0.87×10^{19} and 0.61×10^{19} Ω^{-1} m^{-1} s^{-1} at higher temperatures for $KZnI_3$ and $KSnI_3$, respectively. The $KZnI_3$ demonstrates the highest conductivity overall. The mixed compositions ($KSn_{0.75}Zn_{0.25}I_3$, $KSn_{0.5}Zn_{0.5}I_3$, and $KSn_{0.25}Zn_{0.75}I_3$) show lower electrical conductivity compared to the pure end-members. This reduction in conductivity is typically attributed to the introduction of alloy scattering disorder by mixing Sn and Zn atoms, which impedes the transport of charge carriers. The electrical conductivity for all compositions increases with temperature, indicating a semiconducting or thermally-activated transport mechanism.

3.5.3 Electronic conductivity (K_e). The total thermal conductivity (K) of a material is consists of the lattice thermal conductivity (k_L), which is caused by vibrations in the lattice structure, and the electronic conductivity (k_e), which is caused by the motion of charge carriers.[81] Fig. 8(c) shows the temperature-dependent electronic conductivity for the $KSn_{1-x}Zn_xI_3$ compounds. In all compositions, K_e increases steadily with temperature, reflecting thermally activated semiconducting transport. The two pure phases, $KSnI_3$ and $KZnI_3$ exhibit the highest K_e values across the entire temperature range. At 950 K, $KZnI_3$ reaches $\sim 1.08 \times 10^{14}$ (m^{-1} k^{-1} s^{-1}), and $KSnI_3$ reaches $\sim 0.51 \times 10^{14}$ (m^{-1} k^{-1} s^{-1}) at 800 K, confirming their superior carrier mobility and reduced scattering in the structurally ordered lattice.

In contrast, the mixed alloys typically display lower electronic conductivity. For example, the electronic conductivity of $KSn_{0.5}Zn_{0.5}I_3$ reduces to 0.39×10^{14} (m^{-1} k^{-1} s^{-1}) at elevated temperatures due to alloy-induced disorder. This introduces potential variation and increases electron–phonon and point-defect scattering. The same trend is seen at 300 K as both $KZnI_3$ and $KSnI_3$ have conductivity greater than that of the respective alloy compositions, indicating that the K_e follows the same hierarchy as the σ in Fig. 8(b). This phenomenon demonstrates that structural ordering in the pure compounds results in significantly higher electronic conductivity than does disorder in the mixed alloys.

3.5.4 Lattice thermal conductivity (K_L). Fig. 8(d) shows the variation of lattice thermal conductivity (K_L) with temperature. For all compositions, K_L decreases continuously as temperature increases. This is a characteristic signature of phonon–phonon scattering, which becomes more effective at high temperature. Among the perovskite compounds, $KZnI_3$ shows the highest K_L, maintaining values near 2.0 W m^{-1} K^{-1} at low temperatures. Its relatively strong lattice stiffness permits more efficient phonon propagation. Elements that are smaller in size usually have higher lattice thermal conductivity due to lower phonon–phonon scattering. Conversely, the reverse effect occurs for atoms with a larger size.[82] For this reason, the compositions with a high percentage of Zn, $KZnI_3$, and $KSn_{0.25}Zn_{0.75}I_3$ have higher lattice thermal conductivity.

The mixed alloys exhibit reduced K_L values, with $KSn_{0.75}Zn_{0.25}I_3$ showing the lowest thermal conductivity among all compositions. This reduction originates from enhanced alloy scattering, where mass-fluctuation and strain-field disorder significantly shorten phonon mean free paths. Although lower K_L is beneficial for increasing ZT, the alloys do not show improved thermoelectric performance because their PF values are drastically reduced. Thus, the thermal conductivity reduction alone is insufficient to compensate for the degradation in electronic transport.

3.5.5 Power factor (PF = $S^2\sigma$). The calculated temperature dependence of the power factor (PF) is shown in Fig. 8(e). A high PF is essential for achieving a high ZT, as it couples the Seebeck coefficient with electrical conductivity. The $KZnI_3$ exhibits the highest power factor, increasing continuously with temperature and approaching $\sim 4.22 \times 10^{11}$ Wm^{-1} K^{-2} s^{-1} at 950 K temperature. This remarkable function can be explained by the simultaneous presence of good electrical conductivity and a moderately high Seebeck coefficient. The combination of these two qualities is rarely combined, but would provide an outstanding combination for a thermoelectric application. The $KSnI_3$ has the second highest PF value of 2.33×10^{11} Wm^{-1} K^{-2} s^{-1} at elevated temperatures. The large Seebeck value is a major contributor in this behavior, but its electrical conductivity remains lower than that of $KZnI_3$.

For the intermediate alloys studied ($x = 0.25, 0.5, 0.75$), the measurements show a significantly reduced PF within the temperature range of 100 K to 1000 K. Disorder in the alloy structure leads to decreased mobility of carriers through alloy scattering and therefore leads to reduced S. Thus, the value of $S^2\sigma$ is significantly less than that of the pure compounds demonstrating the need for structural and electronic coherence across the pure compounds in order to achieve high performance transport. Finally, $KZnI_3$ and $KSnI_3$, as pure end compounds, retain superior pathways for carrier transport compared to disordered mixed alloys.

3.5.6 Figure of merit (ZT). Fig. 8(f) shows the temperature dependency of the figure of merit, which synthesizes all the key thermoelectric properties (S, σ, K_e, K_L) and thereby measures the efficiency of a thermoelectric material. All compositions showed a monotonic increase in ZT as the temperature increased, meaning higher thermoelectric performance at high temperatures. The two highest ZT values are exhibited by the pristine $KSnI_3$ and $KZnI_3$ at high-temperatures, ZT is 1.01 at 800 K, and ZT is 1.27 at 950 K, respectively. The thermoelectric performance of $KZnI_3$ is largely dependent upon its crystallography. Prior studies report a ZT of approximately 0.55 at 1000 K for the cubic phase ($Pm\bar{3}m$, no. 221).[83] In comparison, our work on the orthorhombic phase ($Pnma$, no. 62) reveals a substantially enhanced ZT of about 1.27 at 950 K. This exceptional value

results from its high-power factor combined with favorable thermal transport characteristics, including relatively low lattice thermal conductivity with a strong Seebeck coefficient at elevated temperatures.

To better evaluate the significance of this performance, a comparison with the well-established thermoelectric materials is essential. For example, tin selenide (SnSe) is one of the well-known thermoelectric compounds. The single crystal SnSe has one of the highest *ZT* values in the range of 2.2–2.6 at 913 K, and polycrystalline hole-doped SnSe provides $ZT \sim 3.1$ at 783 K temperature.[84] Another renowned thermoelectric material is $Bi_{0.4}Sb_{1.6}Te_3$, used for low temperature thermoelectric applications, which has $ZT \sim 1.25$ at about 100 °C temperature.[84] However, selenium (Se) and tellurium (Te) are rare trace elements compared to K, Zn, and Sn present in $KSn_{1-x}Zn_xI_3$ perovskites. In case of inorganic perovskite materials, the peak value of *ZT* in $CsSnI_3$ and $CsGeI_3$ with the help of n-type doping can be reached to 0.95 and 1.05, respectively, at 700 K temperature.[77] However, the *ZT* value of $CsPbI_3$ is very low; *ZT* of 0.45 can be achieved with p-type doping at 700 K temperature.[77] However, the K present in $KSn_{1-x}Zn_xI_3$ is much more earth-abundant compared to Cs, making these materials more promising from a sustainability perspective.

In the mixed alloys, *ZT* remains significantly lower throughout the temperature range, mainly due to structural shift. The pronounced disorder reduces carrier mobility and increases phonon scattering, thereby lowering PF and deteriorating *ZT*. Although increased phonon scattering can reduce K_L, it is beneficial. The simultaneous suppression of σ and $S^2\sigma$ outweighs this advantage. As a result, alloying compromises the delicate balance required for high efficiency. Overall, the best thermoelectric performance is achieved in the pure compounds. The $KSnI_3$ and $KZnI_3$ are more promising for high-temperature thermoelectric applications. Whereas intermediate zinc concentrations reduce the overall thermoelectric efficiency. The tunability of thermoelectric behavior through Sn/Zn substitution highlights the potential of $KSn_{1-x}Zn_xI_3$ halide perovskites as next-generation, non-toxic, low-cost thermoelectric materials.

4. Conclusion

This study establishes $KSn_{1-x}Zn_xI_3$ ($x = 0, 0.25, 0.5, 0.75, 1$) perovskites as versatile, non-toxic, low-cost materials for thermoelectric energy harvesting and optoelectronic applications. The thermodynamic stability of all compositions is confirmed by their negative formation energies and phonon stability. It is successfully demonstrated that substituting Sn with Zn not only improves mechanical robustness (*E*, *G*, *B*) but also reduces elastic anisotropy (A^U), which reduces micro-crack formation. These findings imply that there is potential to form thin films on a flexible substrate. The study of thermoelectric behavior indicates that the alloying of Zn to Sn results in the reduction of lattice thermal conductivity due to the scattering. This behavior results in a concurrent degradation of the electronic transport properties and a decrease in both the overall power factor and the overall figure of merit values. The thermoelectric performance is the greatest for two pure materials $KSnI_3$ and $KZnI_3$. The $KSnI_3$ has the greatest performance at lower temperatures with a very high Seebeck coefficient of 220–230 μV K^1, and the *ZT* value is 1.01. Meanwhile, $KZnI_3$ archives optimized power factor $\sim 4.22 \times 10^{11}$ W m^{-1} K^{-2} and *ZT* value of 1.27. The HSE06 functional is used to analyze the electronic characteristics Zn-doped $KsnI_3$ materials. This analysis indicates that Zn can effectively engineer bandgaps of the perovskite compounds between 3.01 eV ($KZnI_3$) and 2.34 eV ($KSn_{0.25}Zn_{0.75}I_3$). As both compounds have wide bandgap, they can be used as suitable candidates for UV-visible optoelectronic devices or as the upper layer of tandem solar cells. Doping the perovskites with Zn allows for a systematic change to three important optical constants, such as optical absorption, reflectivity, and extinction coefficient, allowing for tailored light-matter interaction. In summary, Zn-doped $KSnI_3$ perovskites represent a versatile, non-toxic platform. They are particularly promising for specialized optoelectronic applications in the UV-visible range and for high-temperature thermoelectric waste-heat recovery.

Author contributions

U. Ahmed: conceptualization, data curation, methodology, formal analysis, investigation, visualization, validation, writing – original draft, writing – review & editing. A. S. M. S. Rahman: conceptualization, data curation, formal analysis, investigation, methodology, visualization, project administration, validation, supervision, writing – original draft, writing – review & editing. J. A. Jui: visualization, formal analysis, investigation, writing – review & editing. M. A. Ali: Software, validation, writing – review & editing. M. M. Hossain: validation, writing – review & editing. M. M. Uddin: validation, writing – review & editing.

Conflicts of interest

There are no conflicts of interest to declare.

Data availability

Data for this article including structural, electronic, mechanical, optical, and thermoelectric properties data, are available from the Zenodo repository (https://doi.org/10.5281/zenodo.18755200).

Acknowledgements

This work was conducted at the ACMRL in the Department of Physics at CUET, which was established with the aid of a grant (grant number: 21-378 RG/PHYS/AS_G -FR3240319526) from UNESCO-TWAS and the Swedish International Development Co-operation Agency (SIDA). The views expressed herein do not necessarily represent those of UNESCO- TWAS, SIDA, or its Board of Governors.

References

1 A. S. A. Ahmed, F. S. M. Hashem, A. B. A. El-Adasy and T. A. Seaf El-Nasr, *RSC Adv.*, 2025, **15**, 23266–23301.
2 R. Singh, S. Dogra, S. Dixit, N. I. Vatin, R. Bhardwaj, A. K. Sundramoorthy, H. C. S. Perera, S. P. Patole, R. K. Mishra and S. Arya, *Hybrid Adv.*, 2024, **5**, 100176.
3 H. Ma, T. Lu, X. L. Shi, M. Li, S. Huo, P. Song, Z. G. Chen and M. Hong, *Prog. Mater. Sci.*, 2026, **158**, 101619.
4 C. Asker, C. Pipitone, F. Ursi, K. Chen, A. G. Ricciardulli, E. S. Suena Galindez, S. Luong, P. Samorì, M. Reece, A. Martorana, F. Giannici and O. Fenwick, *J. Mater. Chem. A*, 2025, **13**, 26009–26018.
5 A. Kojima, K. Teshima, Y. Shirai and T. Miyasaka, *J. Am. Chem. Soc.*, 2009, **131**, 6050–6051.
6 P. V. Kamat, *ACS Energy Lett.*, 2025, **10**, 896–897.
7 J. Li, H. L. Cao, W. Bin Jiao, Q. Wang, M. Wei, I. Cantone, J. Lü and A. Abate, *Nat. Commun.*, 2020, **11**, 310.
8 A. S. M. Sayem Rahman and K. M. Shorowordi, *Mater. Sci. Semicond. Process.*, 2025, **186**, 109114.
9 S. Mansouri, K. Zeghdar, L. Dehimi, F. Pezzimenti, R. Chakma, A. M. S. Alhuthali, A. Mohammad, A. A. Aly, N. Badi, M. H. H. Mahmoud, R. Haldhar and M. K. Hossain, *J. Phys. Chem. Solids*, 2026, **211**, 113494.
10 K. Debnath, M. Debbarma, S. Das and S. Chattopadhyaya, *Comput. Condens. Matter*, 2026, **46**, e01204.
11 R. Kundara and S. Baghel, *Mater. Sci. Eng., B*, 2024, **307**, 117536.
12 S. Wang, X. Zhang, W. Zhu, Z. Tang, J. Liu, H. Zhang, L. Ding and F. Hao, *Appl. Surf. Sci.*, 2022, **602**, 154393.
13 M. Liu, H. Pasanen, H. Ali-Löytty, A. Hiltunen, K. Lahtonen, S. Qudsia, J. H. Smått, M. Valden, N. V. Tkachenko and P. Vivo, *Angew. Chem., Int. Ed.*, 2020, **59**, 22117–22125.
14 C. Li, C. Chen, W. Gao, H. Dong, Y. Zhou, Z. Wu and C. Ran, *ACS Nano*, 2024, **18**, 35130–35163.
15 C. Liu, H. Dong, Z. Zhang, W. Chai, L. Li, D. Chen, W. Zhu, H. Xi, J. Zhang, C. Zhang and Y. Hao, *Sol. Energy*, 2022, **233**, 489–493.
16 J. Tong, Q. Jiang, F. Zhang, S. B. Kang, D. H. Kim and K. Zhu, *ACS Energy Lett.*, 2021, **6**, 232–248.
17 Y. Lu, F. Alam, J. Shamsi and M. Abdi-Jalebi, *J. Phys. Chem. C*, 2024, **128**, 10084–10107.
18 W. Zhao, D. Yang, Z. Yang and S. (Frank) Liu, *Mater. Today Energy*, 2017, **5**, 205–213.
19 M. Badrooj, F. Jamali-Sheini and N. Torabi, *Sol. Energy*, 2022, **236**, 63–74.
20 H. Jang, H. Y. Lim, C. B. Park, J. Seo, J. G. Son, T. Song, J. Lee, Y. S. Shin, J. Roe, S. K. Kwak, D. S. Kim and J. Y. Kim, *J. Mater. Chem. A*, 2023, **11**, 10605–10611.
21 Y. J. Guo, J. Su, L. Wang, Z. Lin, Y. Hao and J. Chang, *J. Phys. Chem. Lett.*, 2021, **12**, 3393–3400.
22 A. Kooijman, L. A. Muscarella and R. M. Williams, *Appl. Sci.*, 2019, **9**, 1678.
23 Y. Ou, Z. Lu, J. Lu, X. Zhong, P. Chen, L. Zhou and T. Chen, *Opt. Mater.*, 2022, **129**, 112452.
24 Q. Wei, J. Yin, O. M. Bakr, Z. Wang, C. Wang, O. F. Mohammed, M. Li and G. Xing, *Angew. Chem., Int. Ed.*, 2021, **60**, 10957–10963.
25 A. Ali, B. Anissa, D. Radouan, N. Al Bouzieh and N. Amrane, *Mod. Phys. Lett. B*, 2025, **39**, 2550156.
26 D. Abdullah and D. C. Gupta, *Sci. Rep.*, 2024, **14**, 12644.
27 X. Song, G. Wang, L. Zhou, H. Yang, X. Li, H. Yang, Y. Shen, G. Xu, Y. Luo and N. Wang, *ACS Appl. Energy Mater.*, 2023, **6**, 9756–9763.
28 A. Aqili, A. Y. Al-Reyahi, S. M. Al Azar, S. Saad Essaoud, M. Elamin Ketfi, M. Maghrabi, N. Al Aqtash and A. Mufleh, *Comput. Theor. Chem.*, 2024, **1238**, 114721.
29 M. Agouri, H. Ouhenou, A. Waqdim, A. Zaghrane, E. Darkaoui, A. Abbassi, B. Manaut, S. Taj and M. Driouich, *Epl*, 2024, **146**, 16005.
30 D. K. Bhat and U. S. Shenoy, *New J. Chem.*, 2020, **44**, 17664–17670.
31 U. S. Shenoy, K. D. Goutham and D. K. Bhat, *Mater. Adv.*, 2022, **3**, 5941–5946.
32 U. S. Shenoy and D. K. Bhat, *J. Mater. Chem. C*, 2020, **8**, 2036–2042.
33 U. S. Shenoy and D. K. Bhat, *J. Alloys Compd.*, 2022, **892**, 162221.
34 D. K. Bhat and U. S. Shenoy, *Mater. Today Phys.*, 2019, **11**, 100158.
35 U. S. Shenoy and D. K. Bhat, *J. Alloys Compd.*, 2021, **872**, 159681.
36 D. K. Bhat and U. S. Shenoy, *J. Alloys Compd.*, 2020, **834**, 155181.
37 N. S. Alsaiari, I. Ahmed, S. Hanf, M. M. Rekha, M. Kundlas, M. Ouladsmane, K. Muhammad and J. Rehman, *J. Inorg. Organomet. Polym. Mater.*, 2025, **35**, 7458–7473.
38 M. Belarbi, *Mater. Sci. Eng., B*, 2025, **313**, 117874.
39 P. Bhuvaneswari and P. Sriramalakshmi, *J. Phys. Chem. Solids*, 2026, **209**, 113245.
40 A. Yousfi, O. Saidani, A. Benmakhlouf, T. Helaimia, A. S. Alsubaie, S. R. Al Ahmed and M. R. Islam, *Sci. Rep.*, 2025, **15**, 37022.
41 G. Kresse and J. Furthmüller, *Comput. Mater. Sci.*, 1996, **6**, 15–50.
42 L. A. Constantin, J. P. Perdew and J. M. Pitarke, *Phys. Rev. B:Condens. Matter Mater. Phys.*, 2009, **79**, 075126.
43 J. Yang, L. Z. Tan and A. M. Rappe, *Phys. Rev. B*, 2018, **97**, 085130.
44 H. Ehrenreich and M. H. Cohen, *Phys. Rev.*, 1959, **115**, 786–790.
45 V. Wang, N. Xu, J. C. Liu, G. Tang and W. T. Geng, *Comput. Phys. Commun.*, 2021, **267**, 108033.
46 G. K. H. Madsen, J. Carrete and M. J. Verstraete, *Comput. Phys. Commun.*, 2018, **231**, 140–145.
47 S. J. Clark, M. D. Segall, C. J. Pickard, P. J. Hasnip, M. I. J. Probert, K. Refson and M. C. Payne, *Z. Kristallogr. Cryst. Mater.*, 2005, **220**, 567–570.
48 K. Momma and F. Izumi, *J. Appl. Crystallogr.*, 2011, **44**, 1272–1276.
49 G. Pindolia, S. M. Shinde and P. K. Jha, *Mater. Chem. Phys.*, 2023, **297**, 127426.

50 C. J. Bartel, C. Sutton, B. R. Goldsmith, R. Ouyang, C. B. Musgrave, L. M. Ghiringhelli and M. Scheffler, *Sci. Adv.*, 2019, **5**, eaav0693.
51 M. M. Rabbi, M. H. Mia, S. S. Saif, U. Ahmed, M. M. Hossain, M. M. Uddin and M. A. Ali, *Comput. Condens. Matter*, 2025, **44**, e01093.
52 R. D. Shannon, *Acta Crystallogr., Sect. A*, 1976, **32**, 751–767.
53 A. E. Fedorovskiy, N. A. Drigo and M. K. Nazeeruddin, *Small Methods*, 2020, **4**, 1900426.
54 M. W. Qureshi, X. Ma, G. Tang and R. Paudel, *Sci. Rep.*, 2021, **11**, 3260.
55 G. Pindolia and S. M. Shinde, *Mater. Sci. Eng., B*, 2023, **297**, 116795.
56 I. Bin Abdul Ghani, M. Khalid, H. Yan, M. Kashif, B. Nawaz and J. Wang, *J. Mater. Sci.*, 2024, **59**, 14547–14572.
57 M. Hilal, B. Rashid, S. H. Khan and A. Khan, *Mater. Chem. Phys.*, 2016, **184**, 41–48.
58 A. S. M. Sayem Rahman and K. M. Shorowordi, *Heliyon*, 2025, **11**, e43425.
59 M. S. Alam, M. Saiduzzaman, A. Biswas, T. Ahmed, A. Sultana and K. M. Hossain, *Sci. Rep.*, 2022, **12**, 8663.
60 M. A. Rahman, R. Khatun, R. Ferdous, D. Chandra Roy, M. Z. Hasan, A. Irfan, M. A. Razzaque Sarker, M. M. Hossain, A. Hossain, S. C. Mouna and S. Sarker, *J. Mater. Res. Technol.*, 2023, **26**, 3840–3862.
61 R. Ahmad and N. Mehmood, *J. Supercond. Novel Magn.*, 2018, **31**, 1577–1586.
62 C. Yang, R. P. Xue, X. Li, X. Q. Zhang and Z. Y. Wu, *Renewable Energy*, 2020, **161**, 836–845.
63 S. A. Dar, R. Sharma, V. Srivastava and U. K. Sakalle, *RSC Adv.*, 2019, **9**, 9522–9532.
64 M. M. Hossain, M. A. Ali, M. M. Uddin, A. K. M. A. Islam and S. H. Naqib, *J. Appl. Phys.*, 2021, **129**, 175109.
65 M. M. Namisi, R. J. Musembi, W. M. Mulwa and B. O. Aduda, *Comput. Condens. Matter*, 2023, **34**, e00772.
66 M. H. Mia, U. Ahmed, S. K. Saha and M. A. Ali, *J. Mater. Res. Technol.*, 2025, **36**, 2468–2484.
67 F. Mouhat and F. X. Coudert, *Phys. Rev. B:Condens. Matter Mater. Phys.*, 2014, **90**, 224104.
68 W. Voigt, *Ann. Phys.*, 1889, **274**, 573–587.
69 A. Reuss, *Z. angew. Math. Mech.*, 1929, **9**, 49–58.
70 R. Hill, *Proc. Phys. Soc., London, Sect. A*, 1952, **65**, 349–354.
71 S. F. Pugh, *London, Edinburgh Dublin Phil. Mag. J. Sci.*, 1954, **45**, 823–843.
72 F. J. Disalvo, *Science*, 1999, **285**, 703–706.
73 G. A. Slack, in *Solid State Physics – Advances in Research and Applications*, 1979, vol. 34, pp. 1–71.
74 D. Narducci, E. Selezneva, G. Cerofolini, S. Frabboni and G. Ottaviani, *J. Solid State Chem.*, 2012, **193**, 19–25.
75 F. Serrano-Sánchez, M. Gharsallah, N. M. Nemes, F. J. Mompean, J. L. Martínez and J. A. Alonso, *Appl. Phys. Lett.*, 2015, **106**, 083902.
76 Y. Dou, X. Yan, Y. Du, J. Xu and D. Li, *J. Mater. Sci.:Mater. Electron.*, 2020, **31**, 4808–4814.
77 U. G. Jong, Y. S. Kim, C. H. Ri, Y. H. Kye and C. J. Yu, *J. Phys. Chem. C*, 2021, **125**, 6013–6019.
78 U.-G. Jong, Y.-S. Kim, C.-H. Ri, Y.-H. Kye and C.-J. Yu, *J. Phys. Chem. C*, 2021, **125**, 6013–6019.
79 T. Ye, X. Wang, X. Li, A. Q. Yan, S. Ramakrishna and J. Xu, *J. Mater. Chem. C*, 2017, **5**, 1255–1260.
80 M. Faizan, G. Zhao, T. Zhang, X. Wang, X. He and L. Zhang, *Acta Phys.–Chim. Sin.*, 2024, **40**, 2303004.
81 J. P. Heremans, V. Jovovic, E. S. Toberer, A. Saramat, K. Kurosaki, A. Charoenphakdee, S. Yamanaka and G. J. Snyder, *Science*, 2008, **321**, 554–557.
82 U. Ahmed, M. M. Hossian, M. M. Uddin, N. Jahan and M. A. Ali, *Mater. Adv.*, 2026, **7**, 403–424.
83 M. Agouri, H. Ouhenou, A. Waqdim, A. Zaghrane, E. Darkaoui, A. Abbassi, B. Manaut, S. Taj and M. Driouich, *A. Lett. J. Explor. Front. Phys.*, 2024, **146**, 16005.
84 C. Zhou, Y. K. Lee, Y. Yu, S. Byun, Z. Z. Luo, H. Lee, B. Ge, Y. L. Lee, X. Chen, J. Y. Lee, O. Cojocaru-Mirédin, H. Chang, J. Im, S. P. Cho, M. Wuttig, V. P. Dravid, M. G. Kanatzidis and I. Chung, *Nat. Mater.*, 2021, **20**, 1378–1384.